

Radio Observations of the Hubble Deep Field South Region IV: Optical Properties of the Faint Radio Population

Minh T. Huynh

Spitzer Science Center, MS220-6, California Institute of Technology, Pasadena CA 91125, USA

mhuynh@ipac.caltech.edu

Carole A. Jackson

Australia Telescope National Facility, CSIRO Radiophysics Laboratory, PO Box 76, Epping, NSW 2121, Australia

Ray P. Norris

Australia Telescope National Facility, CSIRO Radiophysics Laboratory, PO Box 76, Epping, NSW 2121, Australia

Alberto Fernandez-Soto

Grupo de Radioastronomía, Dept. Astronomía, Universitat de Valencia. Av. Dr. Moliner 50, Burjassot, 46100-Valencia, Spain

ABSTRACT

The Australia Telescope Hubble Deep Field-South (ATHDFS) survey of the Hubble Deep Field South reaches sensitivities of $\sim 10 \mu\text{Jy}$ at 1.4, 2.5, 5.2 and 8.7 GHz, making the ATHDFS one of the deepest surveys ever performed with the Australia Telescope Compact Array. Here we present the optical identifications of the ATHDFS radio sources using data from the literature. We find that $\sim 66\%$ of the radio sources have optical counterparts to $I = 23.5$ mag. Deep HST imaging of the area identifies a further 12% of radio sources. We present new spectroscopic observations for 98 of the radio sources, and supplement these spectroscopic redshifts with photometric ones calculated from 5-band optical imaging. The host galaxy colors and radio-to-optical ratios indicate that low luminosity (or “radio quiet”) AGN make up a significant proportion of the sub-mJy radio population, a result which is in accordance with a number of other deep radio studies. The radio-to-optical ratios of the bright ($S_{1.4\text{GHz}} > 1\text{mJy}$) sources is consistent with a bimodal distribution.

Subject headings: surveys — radio continuum: galaxies

1. Introduction

Many massive galaxies in the local universe harbor a super-massive black hole, and this implies that most, if not all, galaxies hosted an AGN at some point in time (Kormendy & Richstone 1995). It is now thought that star formation and AGN are linked by some mechanism collectively known as “AGN-driven feedback” (e.g. Croton et al. 2006). Radio emission can be produced by both AGN and starforming processes, and thus radio surveys provide a unique window to study the cosmic evolution of both these important processes.

Early radio surveys ($S_{1.4\text{GHz}} \gtrsim 100 \text{ mJy}$) found objects with powerful radio emitting jets, which are generally termed "radio-loud" AGN. Recent deep radio surveys have found that the Euclidean-normalised radio source counts flatten below about 1 mJy and this cannot be explained by a population of radio-loud AGN. A non-evolving population of local ($z < 0.1$) low-luminosity radio galaxies (Wall et al. 1986), strongly evolving normal spirals (Condon 1984, 1989), and starburst galaxies (Windhorst et al. 1985; Rowan-Robinson et al. 1993) have all been suggested to explain this new population. The faint radio source counts have been successfully modelled by star-forming galaxies (Seymour et al. 2004; Huynh et al. 2005). However, it has also been shown that low luminosity radio quiet AGN can also contribute to the flattening of the source count at sub-mJy levels (Jarvis & Rawlings 2004).

It is now clear that the sub-mJy population is made up of *both* star-forming galaxies and low luminosity AGN, but surprisingly little is known about the exact mix. This is because the optical counterparts to the radio sources are faint and hence spectroscopic followup is difficult and/or requires massive amounts of telescope time. Pioneering work in the Hubble Deep Field North (HDFN) by Richards et al. (1999) found that roughly 60% of sub-mJy ($S_{1.4\text{GHz}} > 0.04 \text{ mJy}$) sources are associated with bright ($I \sim 22$) disk galaxies, 20% are low-luminosity AGN, and the remaining 20% have no counterpart brighter than $I = 25$. Deep Advanced Camera for Surveys (ACS) imaging ($i_{775} < 27$) of the Great Observatories Origins Deep Survey (GOODS) South field identified optical counterparts to 90% of the faint ($S_{1.4\text{GHz}} > 0.06 \text{ mJy}$) radio sources, and about 60% of the GOODS radio sources with spectroscopic information have a spectrum consistent with star formation processes (Afonso et al. 2006). Simpson et al. (2006) find that 90% of $S_{1.4\text{GHz}} > 0.1 \text{ mJy}$ radio sources are identified to $R \sim 27$ in the Subaru/XMM-Newton Deep Field and show that faint and bright radio sources have similar optical colors. This suggests that many of the faint radio sources are passively evolving ellipticals. Using a highly spectroscopically complete (70%) sample of faint radio sources in the HDFN, Barger et al. (2007) confirmed that the optical hosts do not vary much with redshift or radio flux density. The optical host properties, coupled with X-Ray information, provide evidence for a significant proportion of low luminosity or obscured AGN in the faint radio source population (Simpson et al. 2006; Barger et al. 2007). Recent work using radio-based properties such as morphology, the near-IR-to-radio flux density ratio, the mid-IR-to-radio flux density ratio, and radio luminosity, has found that AGN still contribute a third of the total 1.4 GHz source counts at the faintest flux densities ($\sim 50 \mu\text{Jy}$) (Seymour et al. submitted).

The Hubble Deep Field South (HDF-S) is an ideal field for studying radio sources because of the wealth of publicly available data. This field has been studied in wavelengths from the radio to UV-optical, and spectroscopic and photometric redshifts are available for thousands of galaxies in the HDF-S and surrounding regions (Teplitz et al. 2001; Rudnick et al. 2001; Labb   et al. 2003).

Radio observations of the HDF-S were made between 1998 and 2001 with the Australia Telescope Compact Array (ATCA) using all four available frequency bands. Between 100 and 300 hr of observing at each band yielded images at 1.4, 2.5, 5.2, and 8.7 GHz with maximum sensitivities of $\sim 10 \mu\text{Jy rms}$. A detailed description of the observations, data reduction, and initial results was given by Norris et al. (2005) (hereafter Paper I). The full 1.4 GHz catalog and radio source counts were presented in Huynh et al. (2005) (hereafter Paper II). The 2.5, 5.2 and 8.7 GHz catalogs were presented in Huynh et al. (2007a) (hereafter Paper III).

In this paper we present the optical properties of the Australia Telescope Hubble Deep Field South (ATHDFS) radio sources. This paper is organized as follows. In Section 2 we summarise the existing radio and optical images, and present the optical counterparts to the ATHDFS radio sources. Spectroscopic observations by our team and others are presented in Section 3. In Section 4 we present the photometric redshifts

derived from the optical imaging. We discuss the photometric properties of the faint radio population in Section 5.

We assume a Hubble constant of $71 \text{ km s}^{-1} \text{ Mpc}^{-1}$, $\Omega_M = 0.27$ and $\Omega_\Lambda = 0.73$ throughout this paper.

2. Imaging Data

2.1. Radio

The radio observations and data reduction are detailed in Papers I to III, but here we provide a brief summary. The observations consist of single pointings centered on R.A. = $22^{\text{h}}33^{\text{m}}25.96^{\text{s}}$, decl. = $-60^{\circ}38'09.0$ (J2000.0) (1.4 and 2.5 GHz), and R.A. = $22^{\text{h}}32^{\text{m}}56.22^{\text{s}}$, decl. = $-60^{\circ}33'02.7$ (J2000.0) (5.2 and 8.7 GHz). The 5.2 and 8.7 GHz observations are centered on the HST WFPC field, while the 1.4 and 2.5 GHz observations were pointed halfway between the WFPC field and a bright confusing source to allow the bright source to be well cleaned from the 1.4 and 2.5 GHz images.

We used a wide variety of ATCA configurations to maximize u-v coverage. The correlator was set to continuum mode (2×128 MHz bandwidth), with each 128 MHz bandwidth divided into 32×4 MHz channels. The primary flux density calibrator is PKS B1934-638, while secondary gain and phase calibrations were taken throughout our observations using both PKS B2205-636 and PKS B2333-528.

The final images have a maximum sensitivity of 11.0, 10.4, 7.8, 11.0 $\mu\text{Jy rms}$ at 1.4, 2.5, 5.2 and 8.7 GHz, respectively. The size of the images vary because the primary beam of the ATCA is smaller at high frequencies. We catalogued 1.4 GHz sources to 20 arcmin distance from the image center, while for 8.7 GHz we reach 3.5 armin distance. Sources were catalogued to a local S/N ratio of 5σ at 1.4., 5.2 and 8.7 GHz, and 5.5σ at 2.5 GHz. A consolidated catalogue with the radio sources matched across all four bands was presented in Paper III, comprising 473 individual sources.

2.2. CTIO Wide Field Images

Palunas et al. (2000) observed the Hubble Deep Field South (HDFS) region using the Big Throughput Camera (BTC) on the CTIO 4 m during September 1998. Images were taken in the Sloan Digital Sky Survey u, Johnson B and V, and Cousins R and I filters. The BTC has a pixel size of 0.43 arcsec and covers a total area of 34.8×34.8 arcmin. Individual exposures were dithered during the observations to fill in the gaps between the BTC CCDs. This resulted in a contiguous field of approximately 44×44 arcmin, centered on the main HDFS.

Catalogues of individual sources were compiled by Palunas et al. (2000) using SExtractor (Bertin & Arnouts 1996). Palunas et al. (2000) fix their photometric system to the Johnson UBV and Cousins RI system (Landolt 1992). The sensitivity of the images differ, with the 5σ detection limits for point-like objects in each band range quoted as $24 < u < 25$, $25.6 < B < 26.6$, $25 < V < 26$, $25 < R < 25.8$, and $23.5 < I < 24.4$. About 50% of the area of each image has a sensitivity limit at the bright end of the range.

We cross-matched the combined ATHDFS catalogue (Paper III) against the CTIO wide field images. To aid in choosing a matching radius we plot the number of candidate matches and the number of chance coincidences against radio-optical offset in Figure 1. Here the number of chance coincidences is determined from the CTIO source density (70,409 catalogued sources over 0.588 deg^2). Figure 1 shows that the number

of chance coincidences matches the number of candidates at a radius of 1.8 arcsec. We therefore choose this distance to be our matching radius.

For the worst case scenario of SN=5 and seeing of 2 arcsec FWHM, we estimate the 1σ CTIO positional uncertainty to be $\sim 0.4''$ in each coordinate. This is similar in scale to the CTIO pixel size. In the ATHDFS, at 1.4 GHz, the average uncertainty is $0.36''$ and $0.43''$ in RA and Dec, respectively. We thus expect the offsets between our radio positions and the CTIO positions to have an rms value of approximately $\sqrt{0.4^2 + 0.4^2} = 0.6''$ in each coordinate, neglecting any offsets between the coordinate frames. Figure 2 shows the offsets between the radio and optical positions, which indicates there is a possible RA offset in the ATHDFS and CTIO image coordinates of ≤ 0.5 arcsec. For probable matches closer than 2 arcsec, the mean offset in RA, δRA , is -0.11 arcsec and the rms is 0.56 arcsec, where $\delta\text{RA} = \text{RA}_{\text{ATHDFS}} - \text{RA}_{\text{CTIO}}$. Similarly, the mean offset in Dec is -0.03 arcsec, with an rms of 0.60 arcsec. We correct for the coordinate shifts between the ATHDFS and CTIO images by shifting the CTIO positions by these mean offsets in RA and Dec before the final matching. The mean offset in RA and Dec after shifting the CTIO coordinates is -0.02 and 0.00 arcsec, respectively, with rms values of 0.56 and 0.64 arcsec (Figure 3). This agrees well with the above predicted rms of $0.6''$ in each coordinate. Our matching radius of 1.8 arcsec is equivalent to about 2.2σ , and so should include $\sim 97\%$ of the true IDs.

The I band CTIO image was examined at all radio positions. In 11 cases the optical counterpart is close to a bright star, so the photometry for these sources is not reliable. These instances are flagged in the catalogue. For radio sources which comprise a multiple component radio source (see Paper II) the optical counterpart maybe positioned between the two or more sources, i.e. at the radio centroid. The two cases where this occurred (multiple sources ATHDFS_J223232.4–603542 and ATHDFS_J223443.9–602739) are shown in Figure 4.

The number of ATHDFS sources with a CTIO optical counterpart is 306. Eight of the radio sources lie outside of the CTIO image area, so out of a possible 465 radio sources, 66% have optical counterparts in the CTIO images. We expect 44 chance coincidences using the CTIO source density of $119,740 \text{ deg}^{-2}$ and total search area of $(\pi * 1.8'^2) \times 473$. To derive another estimate of the number of chance coincidences we shifted the radio source positions north by 0.5 arcmin and re-applied the matching program. From this method we find 55 chance coincidences, which is consistent with our first estimation. We therefore conclude that up to 50/315, or 16%, of our CTIO matches could be spurious.

The results of cross-matching the full ATHDFS catalogue against the CTIO imaging is presented in Table 1. A description of Table 1 is as follows:

Column (1) — ATHDFS source name.

Column (2) — CTIO flag. “YES” indicates there is a CTIO counterpart within the 1.8 arcsec matching radius. “NO” means there is no CTIO counterpart within the 1.8 arcsec matching radius. “S” indicates there is a nearby bright star which may affect the photometry. OUT indicates the source lies outside of the CTIO images.

Column (3) — CTIO source ID, corresponding to the source number from the CTIO catalogue (Palunas et al. APJS, submitted).

Column (4) — U magnitude.

Column (5) — rms error in U magnitude.

Column (6) — B magnitude.

Column (7) — rms error in B magnitude.

Column (8) — V magnitude.

Column (9) — rms error in V magnitude.

Column (10) — R magnitude.

Column (11) — rms error in R magnitude.

Column (12) — I magnitude.

Column (13) — rms error in I magnitude.

Column (14) — CTIO photometric redshift.

Column (15) — CTIO photometric redshift uncertainty.

2.3. Hubble Space Telescope Images

Images of the Hubble Deep Field South were obtained by all three instruments on board the Hubble Space Telescope in 1998: the Wide Field Planetary Camera 2 (WFPC2), the Near Infrared Camera and Multi Object Spectrograph (NICMOS), and the Space Telescope Imaging Spectrometer (STIS). The HST observing strategy is described in Williams et al. (2000).

2.3.1. Main Fields

The main deep field WFPC2 observations were centered on RA = 22 32 56.22, and Dec = −60 33 02.69 (J2000). The WFPC2 observations consist of exposures in four broadband filters: F300W, F450W, F606W, and F814W, which have central wavelengths of approximately 2940, 4520, 5940, and 7920 Å, respectively. These filters are the HST analogues of the well known Johnson U, B, V and Cousins I filters. The 10σ limiting AB magnitude of the WFPC2 observations are 26.8, 27.7, 28.3 and 27.7 for the F300W, F450W, F606W, and F814W filters, respectively (Casertano et al. 2000).

The Near Infrared Camera and Multi Object Spectrograph (NICMOS) instrument was used to obtain deep near infrared images. Imaging was performed in three NICMOS filters (Williams et al. 2000): F110W, F160W and F222W. These filters correspond roughly to J (F110W), H (F160W) and K (F222W). The NICMOS field is centered at RA = 22 32 51.75, and Dec = −60 38 48.20 (J2000). The sensitivity, while not uniform over the whole image, reaches a limiting F160W (H) AB magnitude of ≈ 28.7 and F222W (K) AB magnitude of ≈ 24.8 (Yahata et al. 2000).

The Space Telescope Imaging Spectrometer (STIS) observations were centered on the STIS QSO (Sealey et al. 1998) at RA = 22 33 37.5883, and Dec = −60 33 29.128 (J2000). The imaging was performed mainly with the 50CCD detector in a filterless mode which provides a wide (2500 Å FWHM) bandpass centered at approximately 5800 Å. Rough color information was obtained by observations with the F28X50LP filter which is a long pass filter beginning at approximately 5500 Å. These images cover a square region totally 0.83 arcmin² with a resolution of 0.05 per pixel. The filterless 50CCD images correspond roughly to $V + I$ and reach a depth of 29.4 AB magnitudes (Gardner et al. 2000).

Figures 5 to 7 show the full HST deep images overlaid with ATHDFS 1.4 GHz contours. Four of the ATHDFS radio sources lie within the WFPC2 field, one is in the NICMOS field, and two lie in the STIS field (Tables 2 to 4). All four sources within WFPC have a counterpart within 1.5 arcsec, and the others have counterparts within 0.5 arcsec. Using the WFPC2 source density of 2657 objects over 5.07 arcmin², we expect only one of these alignments, at most, is due to chance. The grey scale postage stamp images of each source are presented in Figure 8 .

2.3.2. Flanking Fields

In addition to the main deep field exposures, a series of shallower observations were carried out over 27 orbits of the HST. Nine two-orbit WFPC2 pointings were used to observe a contiguous area of sky between the deep STIS, WFPC2 and NICMOS fields, overlapping both the STIS and NICMOS deep fields (Williams et al. 2000). Each of the WFPC2 flanking field exposures has simultaneous STIS and NICMOS exposures. The WFPC2 observations were performed in the I band (F814W), while the STIS images were with the filterless 50CCD configuration and NICMOS images were in H band (F160W). While sensitivity varies slightly between the images, the average 5σ limiting AB magnitude for the flanking field images is I (F814W) = 26.02, H (F160W) = 26.32, and V + I (50CCD) = 28.24 for the WFPC2, NICMOS and STIS images, respectively (Lucas et al. 2003).

A deep nine-orbit STIS filterless 50CCD image of the main NICMOS field was also obtained as part of the flanking fields program. This was in order to obtain rough color information on NICMOS objects. The STIS image reaches a 5σ AB magnitude of V + I = 29.09 (Lucas et al. 2003). Simultaneous exposures by WFPC2 achieve V (F606W) = 27.79 and I (F814W) = 27.15, and the simultaneous NICMOS imaging depth is J (F110W) = 26.94 and H (F160W) = 26.66 (Lucas et al. 2003).

We cross-matched the positions of our ATHDFS radio sources with the full flanking field catalogues (Lucas et al. 2003). Flanking field objects were considered probable counterparts if the positional offset was less than 3 times the radio positional uncertainty. The largest offset accepted as a match is for ATHDFS_J223307.1–603448, where the WFPC2 counterpart is radially offset from the radio position by 1.96''. In Table 5 we summarise the properties of the counterparts found in the STIS, NICMOS and WFPC2 flanking fields, respectively. Grey scale HST postage stamp images with overlaid radio contours for all flanking field counterparts are presented in Figures 9 to 11.

2.3.3. Analysis of HST Counterparts and Optically Faint Microjansky Sources

In Section 2.2 we found that 66% of our ATHDFS sources are detected by CTIO imaging. In the main WFPC2 field, the HST imaging achieves sensitivities 4.2 mag deeper than CTIO in the F814W (pseudo-I) band. In the flanking fields, the HST goes 2.5 mag deeper in I. Thus, we expect the HST imaging to detect more of our radio sources. The HST imaging can also be used to confirm that the CTIO imaging is sensitive to I = 23.5.

Table 6 lists the CTIO and HST I magnitudes of the ATHDFS sources which lie in the WFPC2 deep and flanking fields. There are thirty five radio sources within this region, and of these, twenty two have CTIO counterparts. Five of the thirteen sources without CTIO counterparts (i.e. I mag > 23.5) are identified in the WFPC2 imaging (F814W < 26.0). If the sample within the WFPC2 deep and flanking fields is representative

of the full ATHDFS radio sample, then 67% of our radio sources are detected to I mag = 23.5 (CTIO limit) and 79% to I mag \sim 26.0 (WFPC2 limit). This is consistent with the HDFN and SSA13 fields, where a sub-mJy radio source identification rate of 80% was achieved for a limit of I mag = 25.0 (Richards et al. 1999).

This implies that there is a sizable proportion of sub-mJy radio sources with very faint optical counterparts ($I_{AB} > 26$). We use the I mag limit to calculate the lower limit to the radio-to-optical ratio (see Section 5.2) of these sources. Table 7 lists the 1.4 GHz flux density and radio-to-optical ratio (R_I) limit for these eight sources. We find that all of these optically unidentified sources have relatively high radio-to-optical ratios ($R_I > 2.5$). Four sources have $R_I > 3$, which meets the criteria for radio-loud AGN discussed in Section 5.2. Redshifts are required before we can firmly rule out star formation processes as the source of the radio emission. However, we do note that these sources maybe similar to the optically faint microjansky sources identified in radio observations of the HDFN and SSA 13 fields (Richards et al. 1999).

Because of their faintness not much is known about optically faint microjansky sources, but Richards et al. (1999) propose several possibilities for the nature of these radio sources: (1) luminous dust-enshrouded starbursts at high redshifts of $z = 1 - 3$, (2) extremely high redshift AGN ($z > 6$), or (3) luminous obscured AGN at $z \gtrsim 2$. Submillimetre observations have shown that a significant fraction of these sources (at least 30%) are dusty starbursts at $1 < z < 3$ (Barger et al. 2000; Chapman et al. 2001, 2003). A large fraction ($\sim 50\%$) of the population also has detectable X-ray emission (Alexander et al. 2001), and the majority of these X-ray detected sources have obscured AGN activity. A stacking analysis performed on the optically faint microjansky sources not detected by current X-ray observations found that their average X-ray properties are consistent with an object like Arp220 lying at $z \sim 1.5$ (Alexander et al. 2001). Recent high resolution radio images suggest optically faint microjansky sources are examples of dusty high redshift starbursts, and some of these seem to be composite sources with an embedded AGN (Muxlow et al. 2005).

3. Spectroscopic Data

3.1. Spectroscopy in Literature

The AAO undertook a public domain redshift survey of the Hubble Deep Field South using the upgraded Low Dispersion Survey Spectrograph (LDSS++). The HDFS LDSS++ targets were selected from deep AAT Prime Focus Imaging to $R < 24$ of a 9×3 arcmin field covering the main WFPC2 and STIS HST fields (Glazebrook et al. 2006). A total of 225 targets were observed simultaneously. The spectra obtained have 8Å spectral resolution and cover the wavelength range from 5300Å to 10700Å. Four radio sources have high quality (2 or more lines) LDSS++ spectra, and we summarise the LDSS++ counterparts in Table 8. The spectra were examined and typed using the same criteria and nomenclature as the 2dF spectroscopy.

Spectroscopy was also obtained at the Very Large Telescope (VLT) using the FORS2 spectrograph in multi-object spectroscopy (MOS) mode. A total of 194 galaxies in the main HDFS and Flanking Fields were targeted during 2000 and 2002. Reliable redshifts, determined from multiple spectral features or the [OII] 3727Å doublet, were obtained for 97 targets (Sawicki & Mallén-Ornelas 2003). Approximately half of all galaxies brighter than $F814W(AB) = 24$ in the HDFS proper were observed, and redshifts obtained for 76%. We cross-matched the ATHDFS radio sources against the Sawicki & Mallén-Ornelas (2003) redshift catalogue. A total of five counterparts were found and Table 9 summarises the results.

3.2. 2dF Optical Spectroscopy

The public domain spectroscopic followup of galaxies in the HDFS and the surrounding region has yielded about 400 redshifts (Vanzella et al. 2002, Sawicki & Mallén-Ornelas 2003, Glazebrook et al. 2006). Only 6 of our radio sources have spectroscopic redshifts from the literature, however. The main factor limiting the spectroscopic completeness is that these redshift surveys were concentrated on the central WFPC2 field and the surrounding HST flanking fields, whereas our radio sources are from a region 40 arcmin in diameter. Hence we undertook wide field spectroscopic observations.

We obtained spectra of the ATHDFS radio sources over two service nights in July 2001 and October 2003 using the multi-fibre 2dF instrument of the Anglo-Australian Telescope (AAT). The 2dF allows the simultaneous acquisition of up to 400 spectra over a 2 degree diameter region of sky. We employed the 2dF-GRS (Colless et al. 2001) observing strategy, which is to use a 300 lines/mm grating at a central wavelength of 5800Å. This yielded low resolution (9Å) spectra over the wavelength range 3800Å to 8000Å. Our data consisted of six consecutive 20-minute exposures, giving a total of 2 hours on source.

The spectra were reduced using the *2dfdr* reduction package, developed by the AAO specifically for 2dF spectra data. We were unable to place a fibre on all targets due to crowding, so higher priority was given to our radio sources with bright ($B < 23$) counterparts. A total of 268 sources from the 1.4 GHz ATHDFS catalogue were targeted. Redshifts were determined by visually inspecting the spectra. Each spectrum was assigned an index, Q , that signifies the quality of the redshift determination. A value of $Q = 3$ indicates three or more lines were identified, so the redshift is very well determined. Two, one or no lines identified are indicated by $Q = 2, 1$ or 0 , respectively. Redshifts were obtained for 98 out of the 268 targeted sources. In Figure 12 we plot B magnitude against 1.4 GHz flux density for the ATHDFS radio sources. From this we can see that the 2dF success rate is almost 100% for all targeted sources brighter than about $B = 22$. Redshifts are much harder to obtain for the fainter sources. In the $B > 23$ cases, the spectra is low SN and the redshift determination only possible by the detection of bright emission lines.

The spectra were also used to classify our radio sources. We divided the spectra into five broad classes:
i) galaxies with absorption line spectra (22, 22%),
ii) starforming galaxies (36,37%),
iii) Seyfert galaxies (6, 6%),
iv) broadline AGN (7, 7%),
v) unclassified objects (27, 28%).

The unclassified objects have at least one identifiable line in their spectrum, but insufficient SN or not enough observed lines to make a classification possible.

The Seyferts were determined by [O III] 5007/H β and [N II]6583/H α diagnostic line ratios. Although the 2dF spectrograph is fibre fed, these line pairs are close in wavelength and thus poor flux calibration will not affect these line ratios significantly. The line ratios of all our starforming and Seyfert objects are plotted in Figure 13 along with the Kewley et al. (2001) classification line. The six Seyferts lie above and to the right of the maximum starburst line.

In Table 10 we present a summary of the 2dF spectroscopy of the ATHDFS sources. Information is provided for the sources with 2dF redshifts. A description of Table 10 is as follows.

Column (1) — ATHDFS source name.

Column (2) — 2dF spectroscopic redshift.

Column (3) — quality of 2dF spectroscopy, as described above.

Column (4) — spectral classification, as described above. ‘abs’ are galaxies with absorption lines, ‘sf’ are starforming galaxies, ‘sy’ indicates Seyferts, ‘BL’ marks broadline AGN, and ‘unc’ means unclassified.

Column (5) — H β line flux, in CCD counts

Column (6) — OIII[5007] line flux, in CCD counts

Column (7) — H α line flux, in CCD counts

Column (8) — NII[6584] line flux, in CCD counts

Column (9) — comments on spectra, including what lines are observed

4. Photometric Redshifts

The majority of our radio sources do not have spectral data, but CTIO imaging provides up to five-band photometry of 67% of the radio sources with which to calculate photometric redshifts. Photometric redshifts were determined using the galaxy template technique by two independent groups: Teplitz et al. (2001) and ourselves. Teplitz et al. (2001) used a template set which consisted of Coleman et al. (1980) spectra augmented with a single bluer synthetic starburst (Bruzual A. & Charlot 1993). They calculated photometric redshifts for objects with a clear detection ($> 3\sigma$) in BVR and either u or I. We adopted the template set of Coleman et al. (1980) spectra plus two starburst galaxy spectra. The two new starburst galaxy spectra were formed by adopting starbursts SB1 and SB2 of Kinney et al. (1996), which have different intrinsic color excess, and extrapolating to ultraviolet and near infrared wavelengths using the recipe from Fernández-Soto et al. (1999).

Teplitz et al. (2001) performed a Monte Carlo simulation to estimate the accuracy of their photometric redshifts. Model galaxy spectra (Bruzual A. & Charlot 1993) of varying metallicity and age were redshifted and random photometric error added. The redshift error from applying the photometric redshift method to the simulated spectra is typically 15 — 20% for $z < 1$ (Teplitz et al. 2001). For galaxies with $z > 1$ the typical residuals in the redshift error are $\Delta z > 0.35$. Also, the failures ($\Delta z > 0.33$) for $z < 1$ simulated galaxies are less than 10%, compared with greater than 40% for $z > 1.33$ objects. The failures in the Teplitz et al. (2001) photometric redshift catalogue are likely to be more numerous, since real data contain a larger variety of galaxies, such as AGN. Nevertheless one can conclude that their photometric redshifts are quite reliable to $z = 1$. The reason for the failure at $z > 1$ is the limitations of the CTIO filter set. The most obvious spectral features for template fitting are the 4000 Å and 912 Å breaks, which fall out of the uBVRI passbands. The 4000 Å is shifted to near infrared for $z > 1$, while the 912 Å is out of the u passband until $z \sim 2.5$. The CTIO photometric redshifts are listed in Table 11.

We expect our photometric redshifts to have similar accuracy, since similar data and techniques are used. A photometric redshift was estimated for the 307 1.4 GHz radio sources with a CTIO counterpart from the CTIO imaging. The photometric redshifts are restricted to $0 < z < 1$, as this is the redshift space effectively probed by the uBVRI filter set. Photometric redshifts of $z = 0$ and $z = 1$ were rejected since the photometric redshift code obviously did not find a fit within the desired range. This occurred for 43 of the sources, so in total we derive 264 photometric redshifts. We list these in Table 11.

To investigate the accuracy of our photometric redshifts we compared them with the spectroscopic ones

obtained on 2dF. Of the 98 objects with 2dF redshifts, 85 have photometric redshifts. We show a comparison of the 2dF spectroscopic versus photometric redshifts in the left panel of Figure 14. We find that only six ATHDFS sources have estimated photometric redshifts which are failures ($\delta z/(1 + z_{\text{spec}}) > 0.2$), indicating a high photometric redshift success rate of 79/85 (93%). Four of these sources are broadline emitting quasars which are not well represented by our galaxy templates. The 79 successful photometric redshifts have a median residual $\delta z/(1 + z_{\text{spec}})$ of 0.008 ± 0.064 . In comparison, there are photometric redshifts from Teplitz et al. (2001) for 87 of the sources with 2dF redshifts. A comparison of Teplitz et al. (2001) and 2dF redshifts is shown in the right panel of Figure 14. The success rate ($\delta z/(1 + z_{\text{spec}}) < 0.2$) of the Teplitz et al. (2001) photometric redshifts is 72/87 (83%). We note that there are eight sources with a spectroscopic redshift $z < 1$ which are erroneously given photometric redshifts $z > 1$ by Teplitz et al. (2001). Also, even though Teplitz et al. (2001) allow photometric redshifts greater than $z = 1$, they successfully estimate the redshift of only 1/6 of the broadline emitting objects at $z > 1$. We therefore deem our photometric redshifts to be more reliable than Teplitz et al. (2001) and use only our photometric redshifts in further analysis.

The photometric redshifts are accurate for the 2dF sample. However, is this likely to be true for the full ATHDFS sample? The sources with 2dF redshifts are the optically brightest of our sources (see Figure 12), so the previous comparison between photometric and spectroscopic redshifts is not from a random selection of the full ATHDFS sample. To estimate the contamination in the photometric redshifts we can combine the results from Teplitz et al. (2001) with ours. Figure 15 shows the comparison of the 209 sources which also have photometric redshifts from Teplitz et al. (2001). In the cases where Teplitz et al. (2001) $z < 1$, which is 185/209 (89%), there is good agreement, and the median $\delta z/(1 + z_{\text{phot}})$ is -0.046 ± 0.097 . The two photometric redshift samples are independent fits, yet they agree ($\delta z/(1 + z_{\text{phot}}) < 0.2$) for $\sim 87\%$ of the sources with Teplitz et al. (2001) redshifts. By design, our photometric redshifts will be wrong for sources that actually lie at $z > 1$, but from Figure 15 we see that sources which are possibly at $z > 1$ (from Teplitz et al. 2001) have a flat distribution in our photometric redshifts, and hence are not biased to a particular redshift. It is not clear whether the Teplitz et al. (2001) redshifts are overestimated or our redshifts underestimated for the discordant cases. However, it is likely that our results are correct for a significant portion of these discordant cases since the Teplitz et al. (2001) results have a 40% failure rate for $z > 1$.

The photometric redshifts of our ATHDFS radio sources are listed in Table 11. A description of the table is as follows:

Column (1) — ATHDFS source name.

Column (2) — Teplitz et al. (2001) photometric redshift.

Column (3) — photometric redshift from this work.

Column (4) — best fit spectral template, as described above.

5. Discussion

5.1. Optical Properties of the Sub-mJy Sample

The magnitude distributions of our matched radio sources, at all five CTIO optical bands, are shown in Figure 16. The R magnitude distribution shows that the number of sources declines between $R = 22$ and $R = 24$, and there are similar decreases in the other passbands. We argue that this is a property of the CTIO

identified ATHDFS radio sources, rather than being caused by incompleteness in the optical imaging, since the drop off in number occurs well above the limiting magnitude of the optical data. The mean magnitude of the optical counterparts to our radio sources is 22.7, 23.0, 22.2, 21.3, 20.4 for the U,B,V,R and I bands, respectively, whereas the limiting magnitude of the CTIO images are 24.0, 25.6, 25.0, 25.0, 23.5 for the same passbands.

In Figure 17 we plot the I band magnitude of the sample against 1.4 GHz flux density. The lower flux density sources seem to have fewer bright ($I \text{ mag} < 19$) optical counterparts. The median I magnitude for sources with $S_{1.4\text{GHz}} > 0.5 \text{ mJy}$ is 0.8 magnitudes brighter than the median I magnitude of the faintest radio sources ($S_{1.4\text{GHz}} < 0.1 \text{ mJy}$). This trend of fainter radio sources having fainter optical hosts was also observed by Afonso et al. 2006 (but see Barger et al. 2007).

We plot the absolute I magnitude versus redshift in Figure 18 for the 266 radio sources with redshift information. The magnitudes are k-corrected using the best fit spectral type from the photometric redshift analysis. For six radio sources there was a 2dF spectroscopic redshift but no photometric type. The k-correction in these cases were determined from a starburst template for the 2dF emission line galaxies (2 total), and an E/S0 template for the 2dF absorption line galaxies (2 total). A further two cases were high redshift ($z > 2$) 2dF broadline emitting quasars, which we k-corrected with a QSO composite template from Francis et al. (1991). The approximate I magnitude limit of 23.5 is shown by the solid line in Figure 18. The host galaxies span a small range in absolute magnitude across the redshift range $0 < z < 1$. We find the median absolute I magnitude for $z < 0.5$ sources is -21.7 , while the median absolute I magnitude for sources at $0.5 < z < 1.0$ is -22.3 . So there maybe a trend towards these radio sources having brighter host galaxies at $0.5 < z < 1.0$, but this trend is very weak.

We show absolute I magnitude versus 1.4 GHz radio power for all radio sources with redshift information in Figure 19. The majority of the radio sources ($\sim 80\%$) lie in the magnitude range -20 to -24 . This corresponds to 1.6 dex in luminosity. In comparison, the radio powers have a wider range of luminosities (about 2 dex encompasses 80% of the sources). The higher redshift sources must have higher radio powers, but the median absolute I magnitude does not change noticeably with redshift (Figure 18). So the optical properties of the host galaxies are not changing as fast as the radio power of the host galaxies (c.f. Barger et al. 2007).

In Figure 20 we plot the restframe B - I colors of the optically identified radio sources in our sample against 1.4 GHz flux density and redshift. The solid, dotted and dashed lines in Figure 20 show the restframe colors of a Coleman et al. 1980 E/S0, Sbc and Irr galaxy, respectively. The host galaxies have colors that span the range between E/S0 to Irr, but have a median color that is Sbc-like. We find little variation in the median color of the host galaxies with either flux density or redshift. This supports the suggestion that the host galaxies of faint radio sources are drawn from the same population as that of bright radio sources (c.f. Barger et al. 2007).

5.2. Radio-to-Optical Ratios

The radio-to-optical ratio of a radio source can give clues to the nature of the radio emission and it has traditionally been used to determine the “radio-loudness” of radio sources (Kellermann et al. 1989). While optically selected samples of quasars have been found to have a wide range of radio flux densities, and thus radio-to-optical ratios (Sramek & Weedman 1980; Condon et al. 1981), it has been suggested that the distribution of this ratio is bimodal (e.g. Kellermann et al. 1989; Stocke et al. 1992). These authors find a

dip in the distribution of 5 GHz to B band flux density ratios at $3 < r = S_{\text{5GHz}}/S_{\text{B band}} < 30$, and formally classify radio sources as radio-loud if they have $r > 10$.

The bimodality of radio-loudness is still controversial, though, with White et al. (2000) claiming no bimodality is seen for a radio-selected sample of optically bright quasars from the FIRST Bright Quasar Survey. However, Ivezić et al. (2002) combined the FIRST survey with deeper SDSS data and found evidence for a bimodality with a minimum in the radio-to-optical ratio between 1 and 10. Ivezić et al. (2002) claim that the FIRST Bright Quasar Survey was biased to radio-intermediate sources with ratios between 1 and 10 because of the brighter $I \lesssim 18$ limit, and hence no bimodality was observed. Moreover, a study of the nuclear region of local Seyferts have found that 60% of them meet the radio-loud $r > 10$ criterion, suggesting that, after removing the effects of the diluting host galaxy, most Seyferts are not radio-quiet (Ho & Peng 2001).

We plot the observed radio-to-I-band flux density ratio against redshift in Figure 21. The I band was selected as it is the reddest filter and hence covers the rest-frame optical regime to the highest redshift. Marked on Figure 21 are ratios from the radio-loud and radio-quiet QSOs from Elvis et al. (1994). We also overplot tracks from local starbursts Arp220 and M82, which have star formation rates of several hundred and tens of $M_{\odot} \text{ yr}^{-1}$, respectively. The radio-to-optical ratio tracks for the starbursts cover the intermediate range of 1–10. We find that the majority of the optically detected radio sources have radio-to-optical ratios in the range 1–100, with a median of $S_{\text{1.4GHz}}/S_{\text{I band}} = 10.6$.

Care must be taken when interpreting the radio-to-optical ratio. At high redshifts we are observing objects at a different cosmological epoch, so they may have broadband SED properties which differ from local objects. For instance, there is evidence that high redshift starbursts and ultraluminous infra-red galaxies (ULIRGs) have SEDs that differ from local analogs (Pope et al. 2006; Huynh et al. 2007b). Also, sources at earlier epochs maybe more dust obscured, which would increase the radio-to-optical ratio. The tracks in Figure 21 are therefore a rough guide only. A further complicating factor is that AGN have variable luminosities. The luminosity of an AGN can change on timescales of minutes (X-ray) to months (radio/optical/infrared) (e.g. Hawkins 2002). The effect of variability in the radio should be reduced since the radio observations were taken over a period of 3 years and any variability is therefore diluted. The optical data, however, was obtained over a period of only three days.

Because of these caveats we choose a conservative approach to using the radio-to-optical ratio as a radio-loudness parameter. We class sources as radio-loud AGN if they have $R_I = \log(S_{\text{1.4GHz}}/S_{\text{I band}}) > 2.5$. A source exceeding this ratio always lies above the radio-loud QSO track for redshifts 0 to 5 (Figure 21). Using this criterion, we identify 44 sources as radio-loud AGN, including the sources with only limits in I magnitude. These sources are listed in Table 12.

One interesting source classified as radio-loud is ATHDFS_J223343.7-603651 which has a 1.4 GHz flux density of 0.070 mJy. This faint source is at the detection limit of the CTIO images, and we have no redshift information for it. In Paper III we quote a radio spectral index of $\alpha_{\text{1.4GHz}}^{2.5\text{GHz}} = -1.14 \pm 0.39$ for this source, and identified it as an ultra-steep spectrum radio source. The radio-loud classification of this source is consistent with it being a high redshift radio galaxy.

The distribution of the radio-to-optical ratio of the I band identified sources is shown in Figure 22. The R_I distribution of sources brighter than 1 mJy shows signs of bimodality, in accordance with Ivezić et al. (2002). Although the small number of sources makes it difficult to accurately determine the shape of the radio-to-optical ratio distribution, we find the number of radio bright sources peaks at $R_I > 2$ and has a dip at $0 < R_I < 1$. If we then assume that most of the optically selected AGN in the HDFS are not detected in

the radio, then these undetected optical AGN have $R_I < 0$ and the unobserved part of the R_I distribution must rise for $R_I < 0$. This is inconsistent with (White et al. 2000), but this previous work only had shallow imaging ($I \sim 18$ th mag compared to our $I = 23.5$ limit). Our sample is radio selected, however, so a complete radio survey of a sample of optically selected AGN is needed to confirm the radio-loud/radio-quiet bimodality of AGN. Sixty percent (31/51) of these radio bright sources have ratios greater than $R_I > 2.5$, meeting our conservative radio-loud criterion.

For the full sample, the radio-to-optical ratio shows no sign of bimodality and has a roughly Gaussian distribution with a peak at $R_I = 0.5 - 1$ (Figure 22). However, we only have I band detections for 66% of the sources, and deeper optical imaging is needed to determine the distribution at $R_I > 2$. The faint radio sources are more radio quiet than bright radio sources (as expected). The R_I distribution for the fainter radio sources also shows an extended tail at high ratios, which means we can not rule out low luminosity AGN in this population. We posit that there maybe a lack of sources with ratios in the region $0 < R_I < 1$ at higher radio flux densities, but starbursts and radio-intermediate AGN increase in number as fainter radio flux densities are probed, so the gap in the R_I distribution between 0 and 1 is filled (see Figure 23). We also note that there is a subsample of radio sources undetected in the I band with high radio-to-optical ratios ($R_I > 1.5$), which are the optically faint microjansky sources discussed in Section 2.3.3. Their ratios imply that they are radio-loud AGN or starbursts with large dust obscuration.

5.3. Radio Power and Redshift Distribution

Radio luminosities for the ATHDFS sources are calculated with the redshifts presented in this paper. In Figure 24 we plot the 1.4 GHz radio luminosity of the ATHDFS radio sources against redshift for the spectroscopic and photometric redshift samples. The galaxies classed as starforming from 2dF spectra have luminosities in the range $\log(P_{1.4\text{GHz}}) \sim 20.5 - 23.5 \text{ W Hz}^{-1}$. The early type galaxies have larger radio powers of $\log(P_{1.4\text{GHz}}) \sim 21.5 - 24.5 \text{ W Hz}^{-1}$. This is expected as the radio emission from early type galaxies is driven by a weak AGN, which is more radio powerful than star formation processes. Also as expected, the broadline AGN are the most powerful radio sources ($\log(P_{1.4\text{GHz}}) \sim 23 - 26 \text{ W Hz}^{-1}$). There is significant overlap in the radio powers of the starforming and early galaxy types, and even broadline AGN can have similar radio powers to the most powerful starbursts. This means that radio power alone cannot be used as a discriminator of source types.

The redshift distribution of our sources with spectroscopic redshifts is shown in Figure 25. The median redshift of the whole spectroscopic sample is 0.34. The starforming galaxies are at similar redshifts to the early type galaxies, with median redshifts of 0.28 and 0.31 for the starforming and early type samples, respectively. We note that there is a lack of both spectroscopic starforming and early type galaxies at $z > 0.5$ because of our survey sensitivity limit. The solid line in Figure 24, which marks the radio power sensitivity of our survey, shows how our radio survey becomes increasingly insensitive to sources with starforming and early type radio powers as higher redshifts are probed. The broadline AGN are detected at both low and moderate redshifts, but only the most powerful ($\log(P_{1.4\text{GHz}}) \gtrsim 24$) are detected at $z > 1$. The highest redshift source is a broadline AGN estimated to be at $z = 3.1$. Finally we note that the unclassified sources are at greater redshifts than the starforming or early type galaxies, with a median redshift of 0.46. The greater distance to these sources make them on average fainter in the optical, and thus the spectroscopy of these sources is of lower quality, as expected.

In Figure 26 we show the photometric redshift distribution of our sources, sorted into best fit template

types. The late type galaxies, Sbc and Scd, show a Gaussian like distribution with a peak at $z = 0.35$ and an extended tail. The distribution of the early type galaxies is similar, with a peak also at $z = 0.35$. Again we argue that the decline in the number of sources in these two samples for $z > 0.5$ is probably because of our survey sensitivity. The starbursts and irregulars appear to have a more uniform distribution than the early or late type samples.

6. Summary

We have cross-matched the ATHDFS radio sources with optical imaging from CTIO. We find 306/465 (66%) of the radio sources which lie within the region covered by the CTIO imaging have counterparts to $I = 23.5$.

The HST imaging was also used to search for optical counterparts to our radio sources. The HST imaging reaches a sensitivity approximately 2.5 mag deeper than the CTIO imaging. This identifies a further ~ 12 percent of sources in the HST region. Thus, the identification rate of sub-mJy radio sources to $I = 26.0$ is estimated to be 79%. A sizable proportion ($\sim 20\%$) are fainter than this and remain optically unidentified. These optically faint microjansky sources, also found in other radio surveys, are thought to be a mix of starbursts at $1 < z < 3$ and high redshift obscured AGN.

We have presented spectroscopic redshifts derived from 2dF spectra for 98 of the radio sources. Where the spectra is of sufficient quality, the sources have been classified as early type, starforming, Seyfert or broadline AGN. The spectroscopic sample consists of 22% early type, 37% late type, and 13% Seyferts or broadline AGN. The median redshift of the sample is $z = 0.34$ and a broadline AGN at $z = 3.1$ has been discovered. Photometric redshifts from 5 band CTIO photometry have also been calculated for 264 ATHDFS sources. A total of 56% (266/473) of the radio sources have redshift information.

Using the available optical information, our main results are as follows.

- The observed I band magnitude of $S_{1.4\text{GHz}} > 0.5$ mJy radio sources is 0.8 magnitudes brighter than the faintest radio sources ($S_{1.4\text{GHz}} < 0.1$ mJy).
- The median restframe $B - I$ color of the optical hosts is consistent with that of a Sbc galaxy.
- There is little variation in the restframe optical colours of the host galaxies with redshift (to $z \sim 1$) or 1.4 GHz flux density. This suggests that faint and bright radio sources have similar host galaxies and that the host galaxies do not evolve much with redshift. It is also further evidence that there is a significant fraction of low luminosity or radio quiet AGN in the sub-mJy radio population.
- Using a conservative radio-to-optical flux density ratio, we conclude 44 of the sources are radio-loud and most likely powered by an AGN. We find that 61% (31/51) of bright radio sources ($S_{1.4\text{GHz}} > 1$ mJy) have a radio-to-optical ratio that fits the radio-loud criterion.
- The distribution of the radio-to-optical ratios of the bright ($S_{1.4\text{GHz}}$) radio sources is consistent with a radio-loud/radio-quiet bimodality. However, complete radio observations of an optically selected sample of AGN are required to confirm the dichotomy. We find no evidence for the radio-loud/radio-quiet bimodality in the full ATHDFS sample, which we believe is due to radio-intermediate starbursts and low luminosity AGN becoming more numerous at sub-mJy flux density levels.

The mid-infrared wavelengths can be good discriminators of star formation versus AGN emission (Lacy et al. 2004; Stern et al. 2005). The HDF-S has been observed in the infrared by the *Spitzer Space Telescope*. Future papers in this series will present the *Spitzer* identifications of the ATHDFS radio sources to further investigate the nature of faint radio sources.

MTH would like to thank Nick Seymour for useful discussions. AFS acknowledges support from MEC project AYA2006-14056 and a "Ramón y Cajal" research contract. The Australia Telescope Compact Array is part of the Australia Telescope, which is funded by the Commonwealth of Australia for operation as a National Facility managed by the CSIRO.

REFERENCES

- Afonso, J., Mobasher, B., Koekemoer, A., Norris, R. P., & Cram, L. 2006, AJ, 131, 1216
- Alexander, D. M., Brandt, W. N., Hornschemeier, A. E., Garmire, G. P., Schneider, D. P., Bauer, F. E., & Griffiths, R. E. 2001, AJ, 122, 2156
- Barger, A. J., Cowie, L. L., & Richards, E. A. 2000, AJ, 119, 2092
- Barger, A. J., Cowie, L. L., & Wang, W.-H. 2007, ApJ, 654, 764
- Bertin, E., & Arnouts, S. 1996, A&AS, 117, 393
- Bruzual A., & Charlot, S. 1993, ApJ, 405, 538
- Casertano, S., et al. 2000, AJ, 120, 2747
- Chapman, S. C., et al. 2003, ApJ, 585, 57
- Chapman, S. C., Richards, E. A., Lewis, G. F., Wilson, G., & Barger, A. J. 2001, ApJ, 548, L147
- Coleman, G. D., Wu, C.-C., & Weedman, D. W. 1980, ApJS, 43, 393
- Colless, M., et al. 2001, MNRAS, 328, 1039
- Condon, J. J. 1984, ApJ, 287, 461
- Condon, J. J. 1989, ApJ, 338, 13
- Condon, J. J., Odell, S. L., Puschell, J. J., & Stein, W. A. 1981, ApJ, 246, 624
- Croton, D. J., et al. 2006, MNRAS, 365, 11
- Elvis, M., et al. 1994, ApJS, 95, 1
- Fernández-Soto, A., Lanzetta, K. M., & Yahil, A. 1999, ApJ, 513, 34
- Francis, P. J., Hewett, P. C., Foltz, C. B., Chaffee, F. H., Weymann, R. J., & Morris, S. L. 1991, ApJ, 373, 465
- Gardner, J. P., et al. 2000, AJ, 119, 486
- Glazebrook, K., Verma, A., Boyle, B., Oliver, S., Mann, R. G., & Monbleau, D. 2006, AJ, 131, 2383

- Hawkins, M. R. S. 2002, MNRAS, 329, 76
- Ho, L. C., & Peng, C. Y. 2001, ApJ, 555, 650
- Huynh, M. T., Jackson, C. A., & Norris, R. P. 2007a, AJ, 133, 1331
- Huynh, M. T., Pope, A., Frayer, D. T., & Scott, D. 2007b, ApJ, 659, 305
- Huynh, M. T., Jackson, C. A., Norris, R. P., & Prandoni, I. 2005, AJ, 130, 1373
- Ivezić, Ž., et al. 2002, AJ, 124, 2364
- Jarvis, M. J., & Rawlings, S. 2004, New Astronomy Review, 48, 1173
- Kellermann, K. I., Sramek, R., Schmidt, M., Shaffer, D. B., & Green, R. 1989, AJ, 98, 1195
- Kewley, L. J., Heisler, C. A., Dopita, M. A., & Lumsden, S. 2001, ApJS, 132, 37
- Kinney, A. L., Calzetti, D., Bohlin, R. C., McQuade, K., Storchi-Bergmann, T., & Schmitt, H. R. 1996, ApJ, 467, 38
- Kormendy, J., & Richstone, D. 1995, ARA&A, 33, 581
- Labbé, I., et al. 2003, AJ, 125, 1107
- Lacy, M., et al. 2004, ApJS, 154, 166
- Landolt, A. U. 1992, AJ, 104, 340
- Lucas, R. A., et al. 2003, AJ, 125, 398
- Muxlow, T. W. B., et al. 2005, MNRAS, 358, 1159
- Norris, R. P., et al. 2005, AJ, 130, 1358
- Palunas, P., et al. 2000, ApJ, 541, 61
- Pope, A., et al. 2006, MNRAS, 370, 1185
- Richards, E. A., Fomalont, E. B., Kellermann, K. I., Windhorst, R. A., Partridge, R. B., Cowie, L. L., & Barger, A. J. 1999, ApJ, 526, L73
- Rowan-Robinson, M., Benn, C. R., Lawrence, A., McMahon, R. G., & Broadhurst, T. J. 1993, MNRAS, 263, 123
- Rudnick, G., et al. 2001, AJ, 122, 2205
- Sawicki, M., & Mallén-Ornelas, G. 2003, AJ, 126, 1208
- Sealey, K. M., Drinkwater, M. J., & Webb, J. K. 1998, ApJ, 499, L135
- Seymour, N., McHardy, I. M., & Gunn, K. F. 2004, MNRAS, 352, 131
- Simpson, C., et al. 2006, MNRAS, 372, 741
- Sramek, R. A., & Weedman, D. W. 1980, ApJ, 238, 435

- Stern, D., et al. 2005, ApJ, 631, 163
- Stocke, J. T., Morris, S. L., Weymann, R. J., & Foltz, C. B. 1992, ApJ, 396, 487
- Teplitz, H. I., Hill, R. S., Malumuth, E. M., Collins, N. R., Gardner, J. P., Palunas, P., & Woodgate, B. E. 2001, ApJ, 548, 127
- Vanzella, E., et al. 2002, A&A, 396, 847
- Wall, J. V., Benn, C. R., Grueff, G., & Vigotti, M. 1986, Highlights in Astronomy, 7, 345
- White, R. L., et al. 2000, ApJS, 126, 133
- Williams, R. E., et al. 2000, AJ, 120, 2735
- Windhorst, R. A., Miley, G. K., Owen, F. N., Kron, R. G., & Koo, D. C. 1985, ApJ, 289, 494
- Yahata, N., Lanzetta, K. M., Chen, H., Fernández-Soto, A., Pascarelle, S. M., Yahil, A., & Puetter, R. C. 2000, ApJ, 538, 493

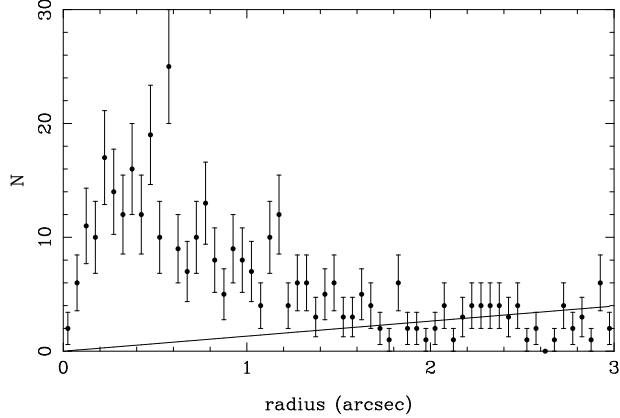


Fig. 1.— Number of candidate CTIO counterparts of ATHDFS sources as a function of radio-to-optical offset. The solid line shows the number of chance coincidences expected from the CTIO source density of 70 409 objects in a 0.588 square degree region.

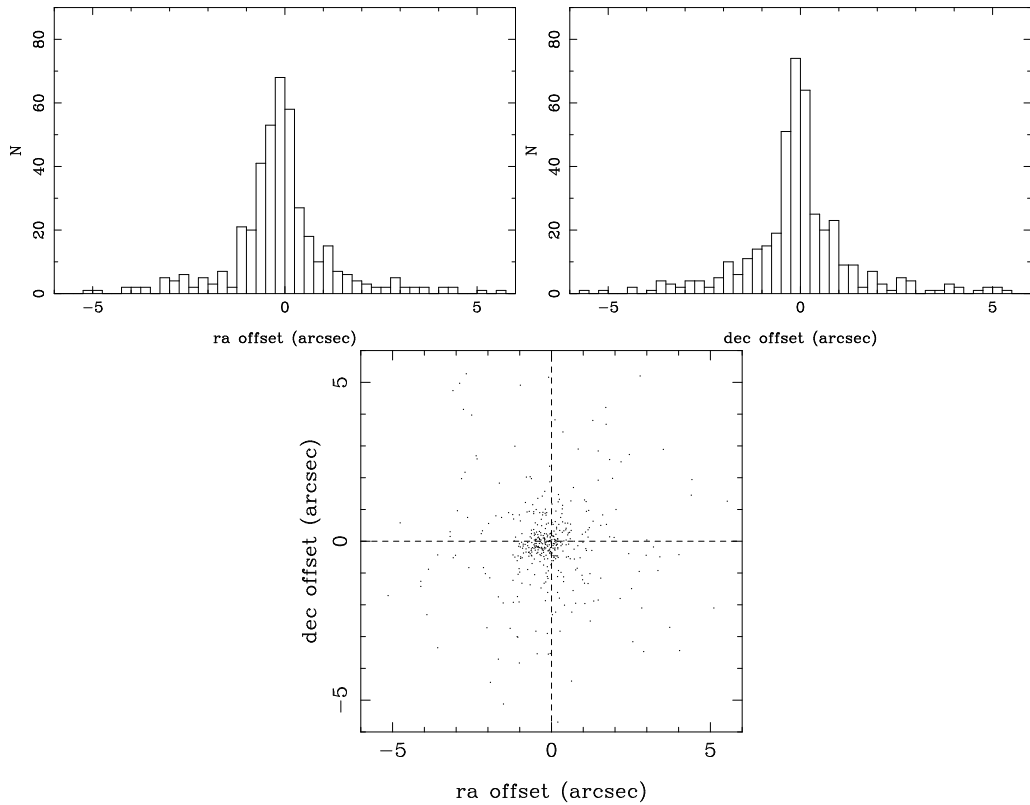


Fig. 2.— Radio to optical position offsets, uncorrected for offset between CTIO and ATHDFS images. Bottom Panel: Distribution of the offsets between the radio and optical positions for all ATHDFS and CTIO sources closer than 6 arcsec. Top Panel: Distribution of the offset in RA and Dec for the CTIO sources closer than 6 arcsec.

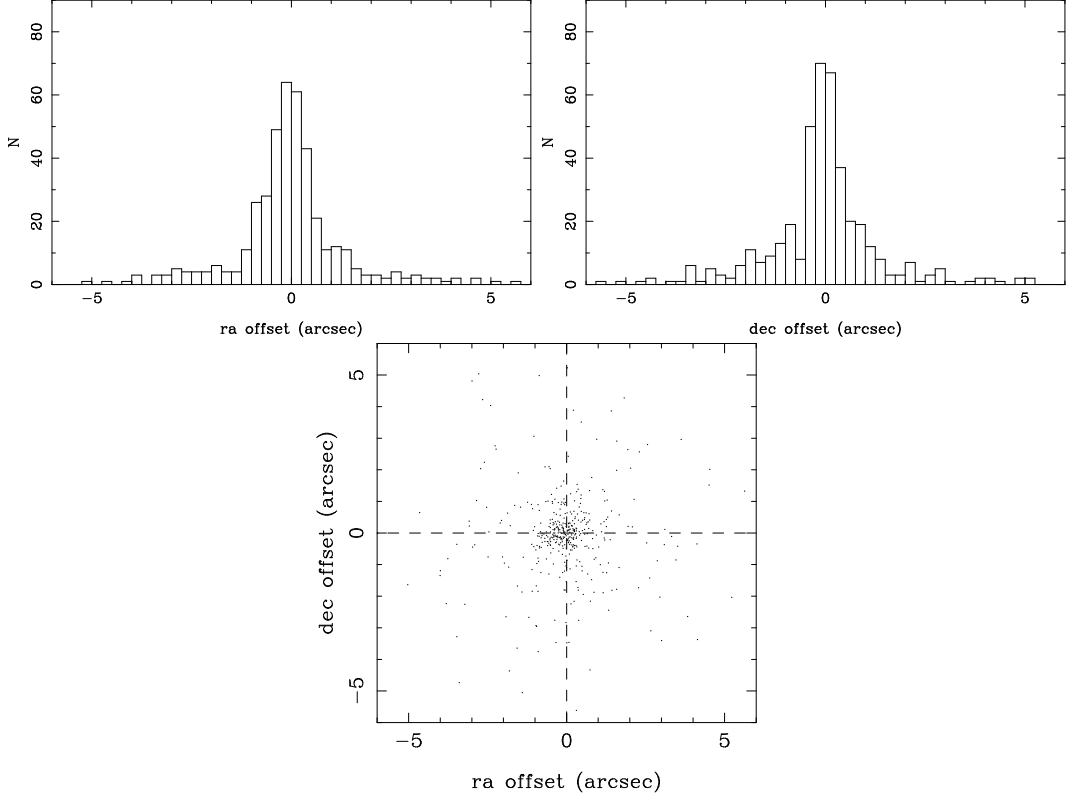


Fig. 3.— Radio to optical position offsets, with CTIO coordinates shifted to correct for offset between CTIO and ATHDFS images. Bottom Panel: Distribution of the offsets between the radio and optical positions for all ATHDFS and CTIO sources closer than 6 arcsec. Top Panel: Distribution of the offset in RA and Dec for the CTIO sources closer than 6 arcsec.

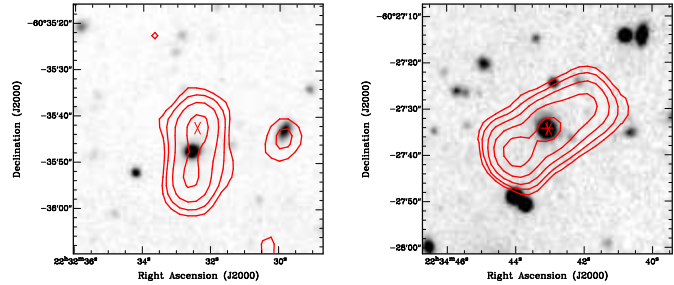


Fig. 4.— Postage stamp images for radio sources with multiple components. The optical counterparts are clearly positioned between the two or more radio source components. The grey scale images are CTIO I band images and the contours are 1.4 GHz flux densities, set at 5, 10, 20, 50, 100 and 200σ . LEFT: multiple radio source ATHDFS_J223232.4-603542. RIGHT: multiple radio source ATHDFS_J223443.9-602739.

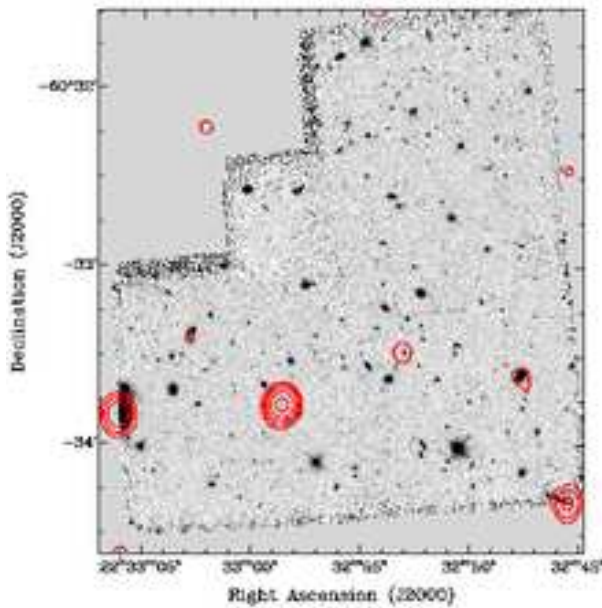


Fig. 5.— HDFS main WFPC2 field - F814W image. The contours are 1.4 GHz flux densities, set at 5, 10, 20, 50, 100 and 200σ .

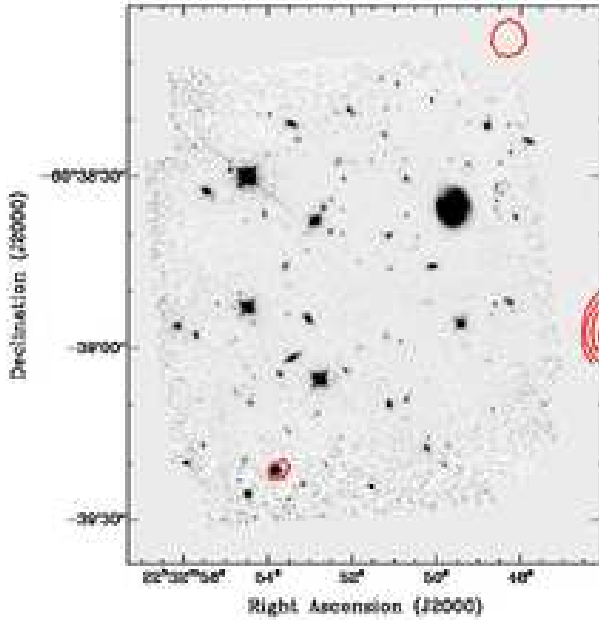


Fig. 6.— HDFS main NICMOS field - F160W image. The contours are 1.4 GHz flux densities, set at 5, 10, 20, 50, 100 and 200σ .

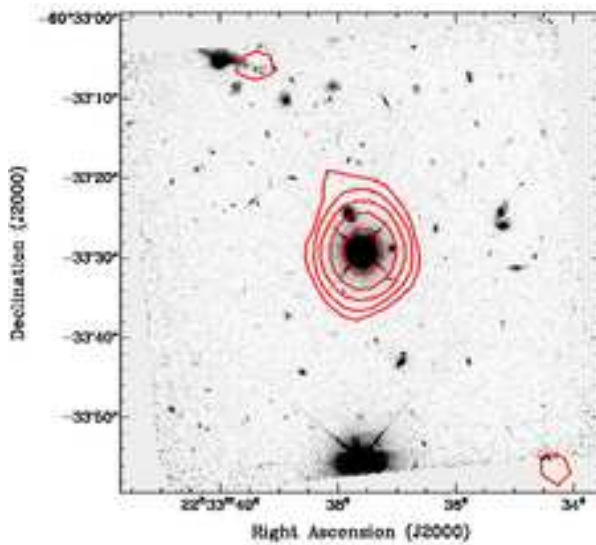
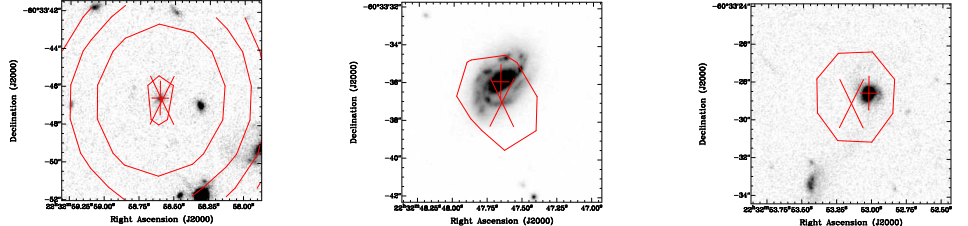


Fig. 7.— HDFS main STIS field - 50CCD image. The contours are 1.4 GHz flux densities, set at 5, 10, 20, 50, 100 and 200σ .

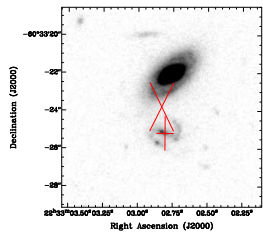
WFPC2 814W



ATHDFS_J223258.5-603346

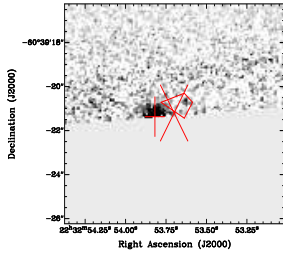
ATHDFS_J223247.6-603337

ATHDFS_J223253.1-603329



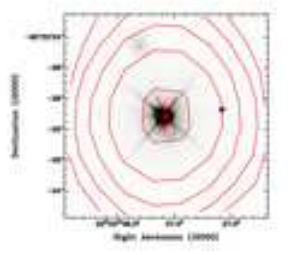
ATHDFS_J223302.8-603323

NICMOS F160W

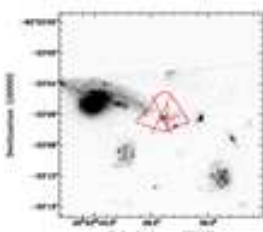


ATHDFS_J223253.7-603921

CROSSES LOCATE



ATHDFS_J223337.5-603329



ATHDFS_J223339.4-603306

Fig. 8.— Grey scale postage stamp images of the HST deep field counterparts to ATHDFS radio sources. Crosses mark the radio position, and the plus signs mark the optical positions. The contours are 1.4 GHz flux densities, set at 5, 10, 20, 50, 100 and 200 σ .

WFPC2 814W

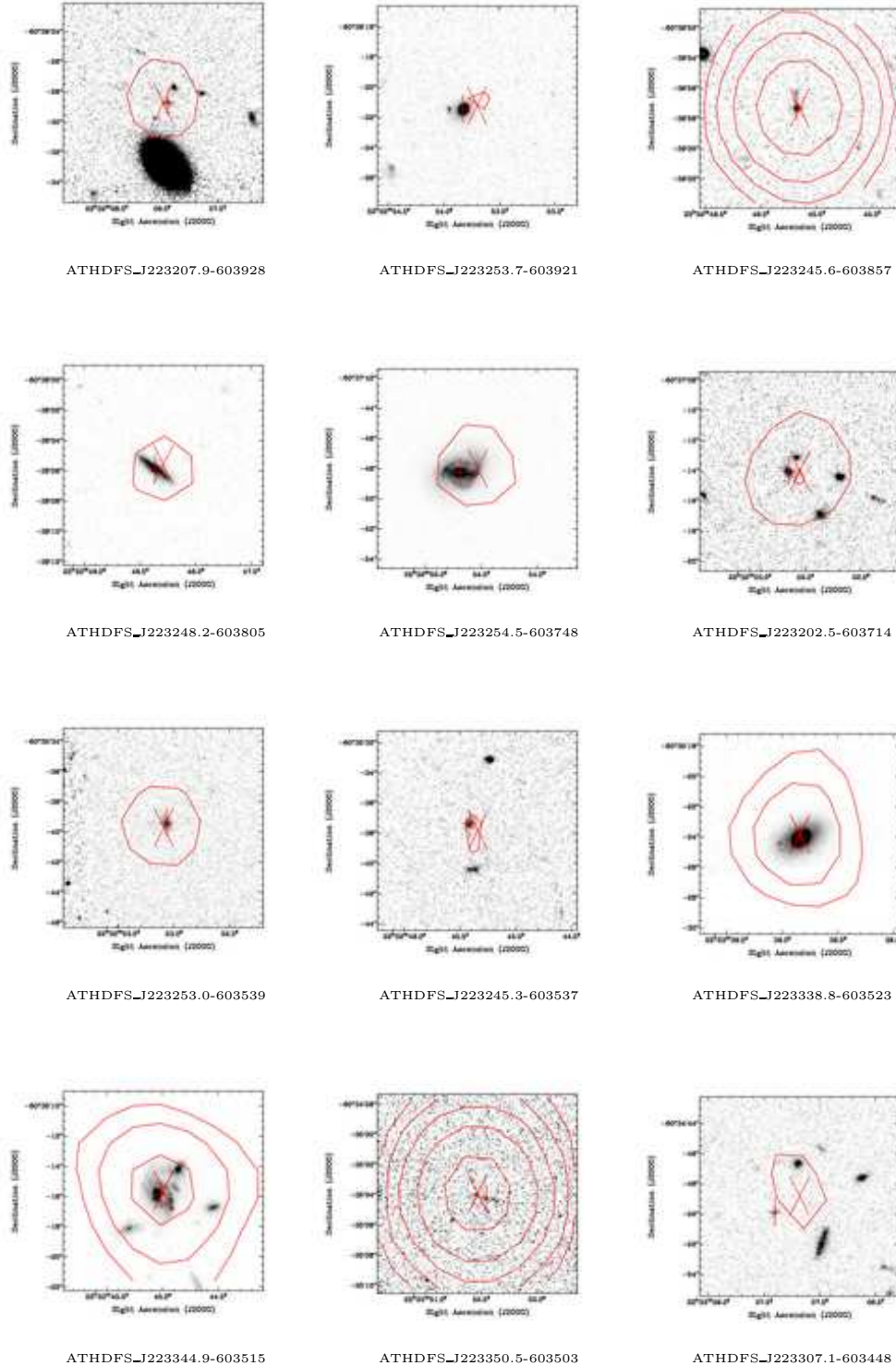


Fig. 9.— Grey scale postage stamp images of the HST WFPC2 flanking field counterparts to ATHDFS radio sources. Crosses mark the radio position, and the plus signs mark the optical positions. The contours are 1.4 GHz flux densities, set at 5, 10, 20, 50, 100 and 200σ .

WFPC2 814W

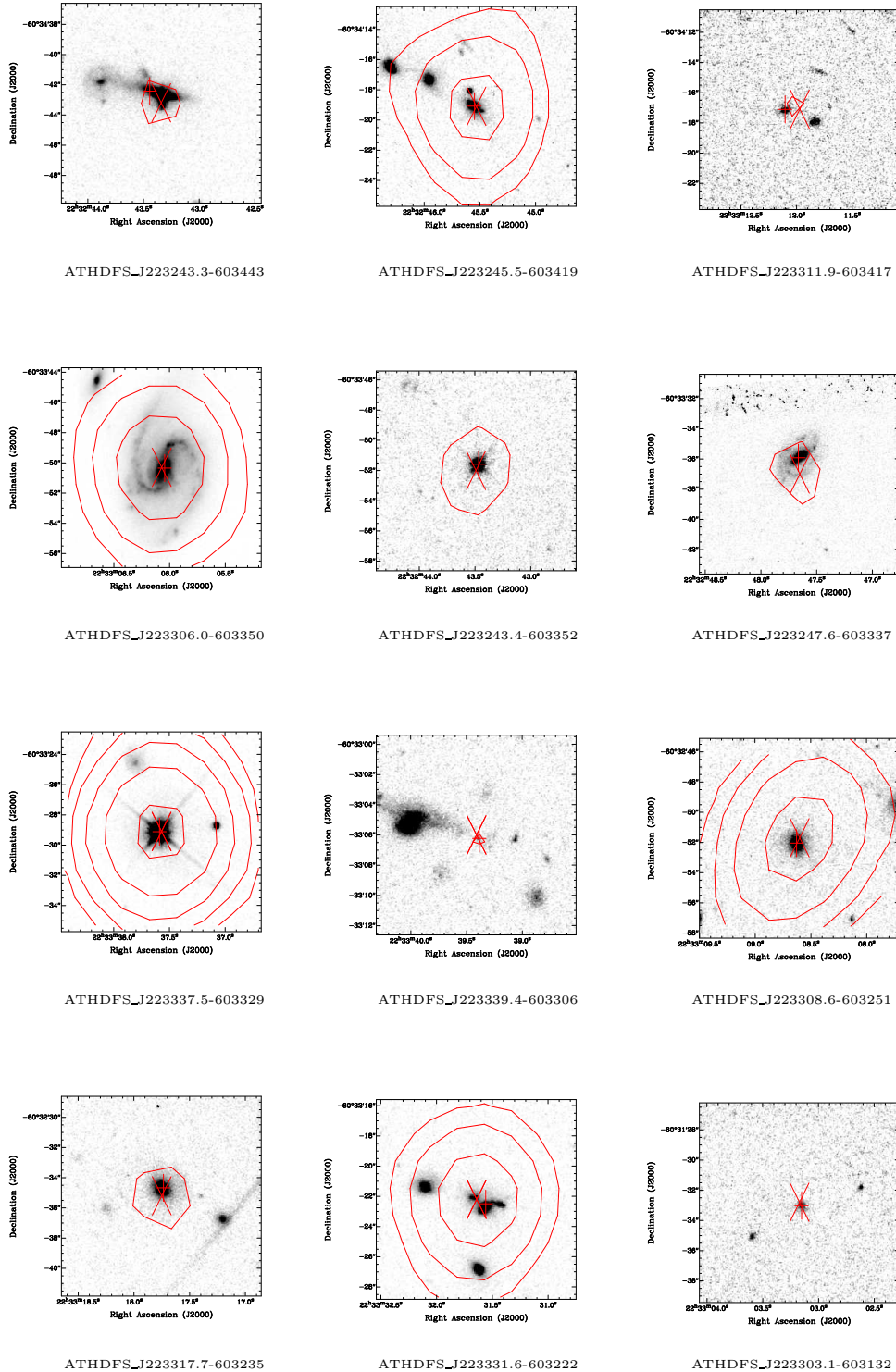


Fig. 10.— More grey scale postage stamp images of the HST WFPC2 flanking field counterparts to ATHDFS radio sources. Crosses mark the radio position, and the plus signs mark the optical positions. The contours are 1.4 GHz flux densities, set at 5, 10, 20, 50, 100 and 200 σ .

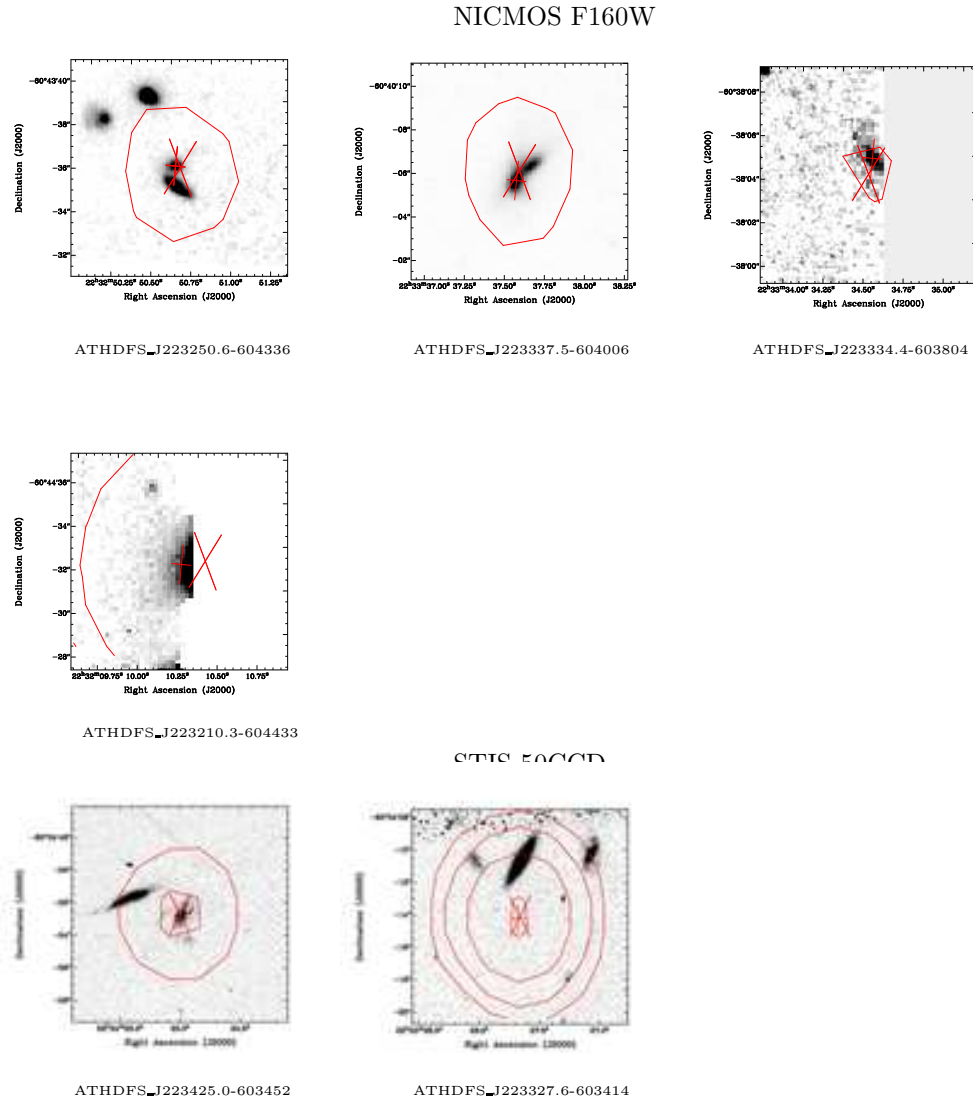


Fig. 11.— Grey scale postage stamp images of the HST NICMOS and STIS flanking field counterparts to ATHDFS radio sources. Crosses mark the radio position, and the plus signs mark the optical positions. The contours are 1.4 GHz flux densities, set at 5, 10, 20, 50, 100 and 200σ .

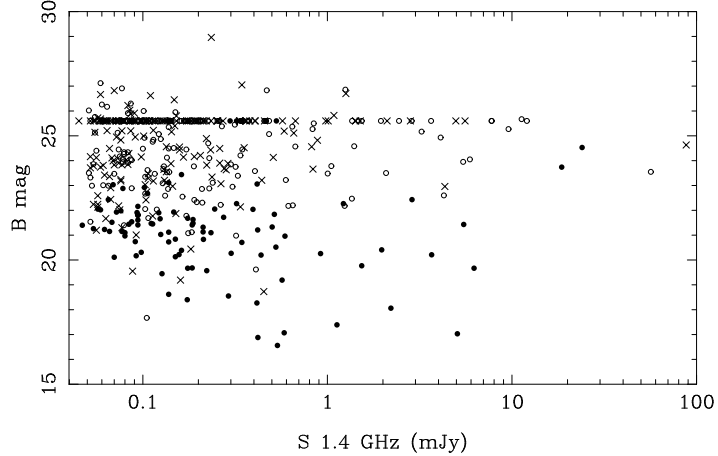


Fig. 12.— B band magnitude versus 1.4 GHz flux density for all ATHDFS radio sources. Filled circles are sources with redshifts successfully obtained from 2dF. Empty circles are 2dF targeted sources, but no redshift was determined. Crosses mark sources which were not targeted in the 2dF observations. Radio sources without optical counterparts are placed at $B = 25.6$, the nominal B band limit of the CTIO observations. We note that in two cases with $B < 20$ no redshift was recorded. The first case is ATHDFS_J223222.4-602532, which is near a star, so the B magnitude of 17.67 is probably overestimated. We suspect the fibre was incorrectly placed for the second case (ATHDFS_J223414.7-604753).

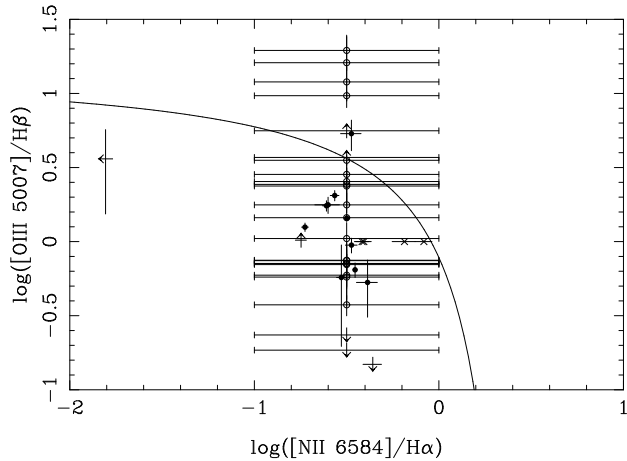


Fig. 13.— Diagnostic line ratio $[N\text{ II}]6583/\text{H}\alpha$ against $[O\text{ III}]5007/\text{H}\beta$ for the 42 narrowline emitting galaxies in our 2dF sample. Filled circles indicate sources where all four lines are detected. Open circles mark high redshift galaxies where the $\text{H}\alpha$ and N II lines are out of the wavelength coverage. For these sources the uncertainty in $[N\text{ II}]6583/\text{H}\alpha$ is marked by large error bars. Crosses mark sources with no detectable $\text{H}\beta$ or $[O\text{ III}]5007$ emission. Arrows indicate upper and lower limits. The solid curve is the theoretical maximum starburst line from Kewley et al. (2001). Starforming galaxies lie below this line, while AGN are found above this line.

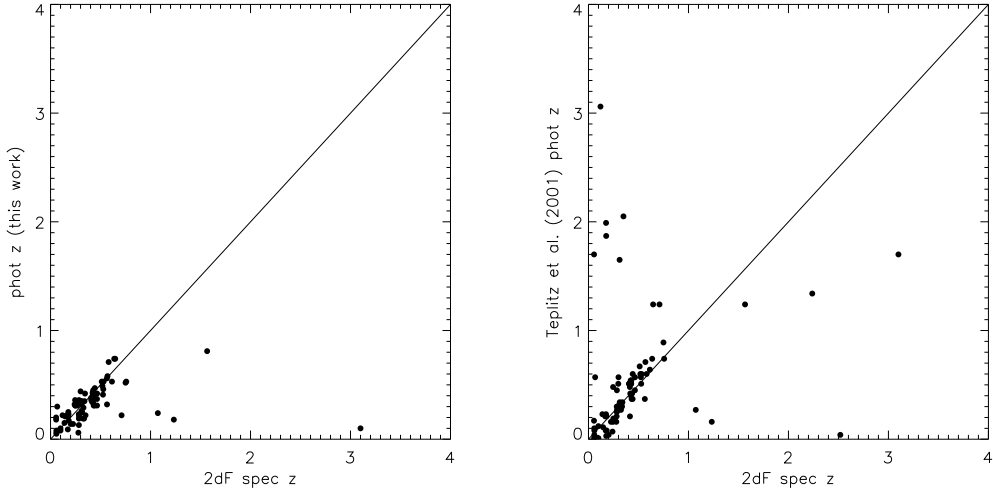


Fig. 14.— LEFT: Comparison of 2dF spectroscopic and our photometric redshifts for the 85 ATHDFS sources that have both. RIGHT: Comparison of 2dF spectroscopic and Teplitz et al. (2001) photometric redshifts for the 88 ATHDFS sources that have both.

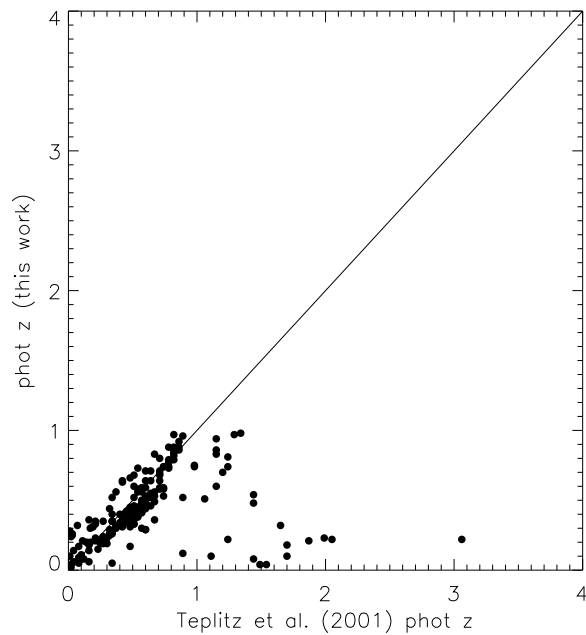


Fig. 15.— Comparison of Teplitz et al. (2001) and our photometric redshifts for the 209 ATHDFS sources that have both.

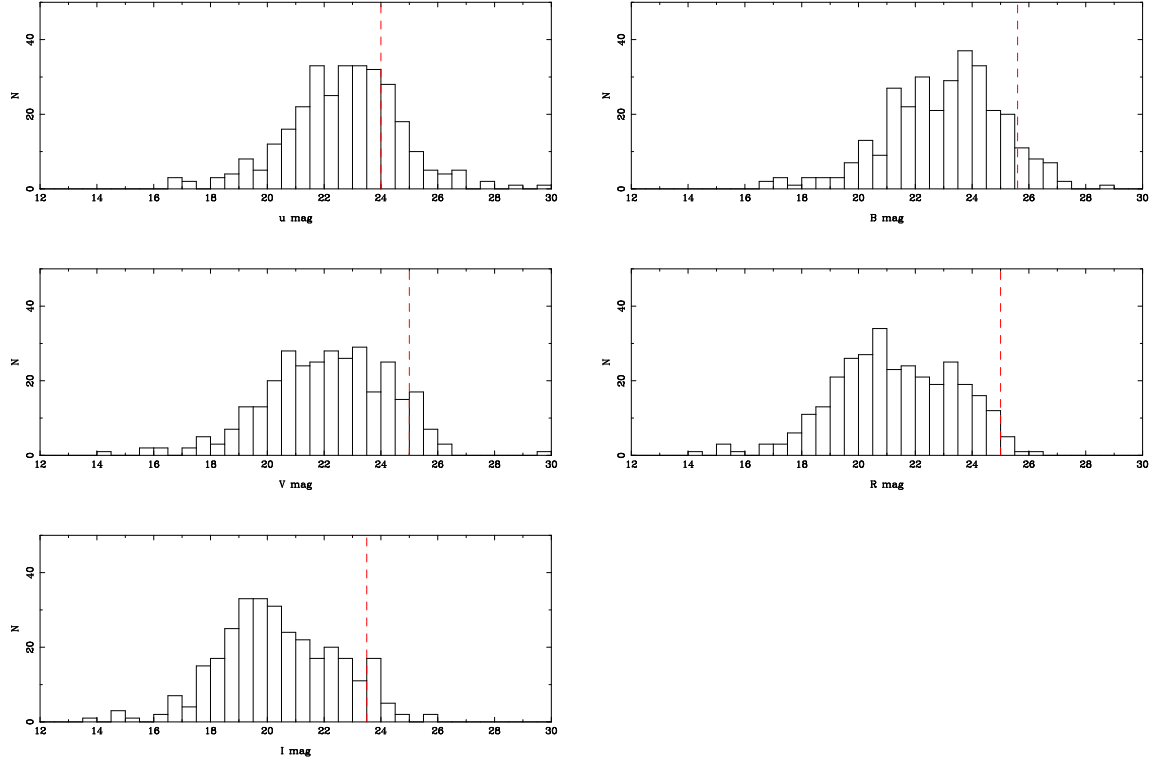


Fig. 16.— uBVRI magnitude distribution of the 315 ATHDFS sources with CTIO counterparts.

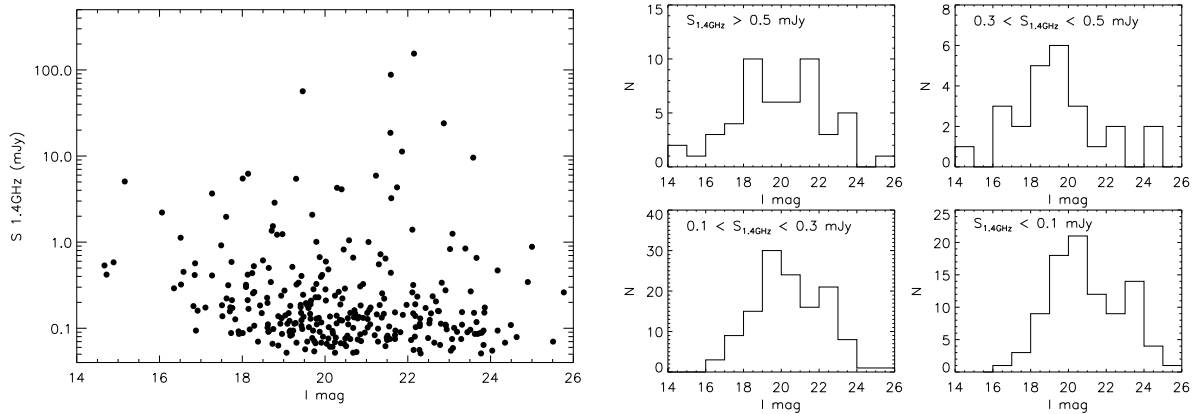


Fig. 17.— Left Panel: The 1.4 GHz flux density versus I magnitude for the radio sources detected in the CTIO I band image. Right Panel: The I magnitude distributions for the radio sources for flux density bins as shown.

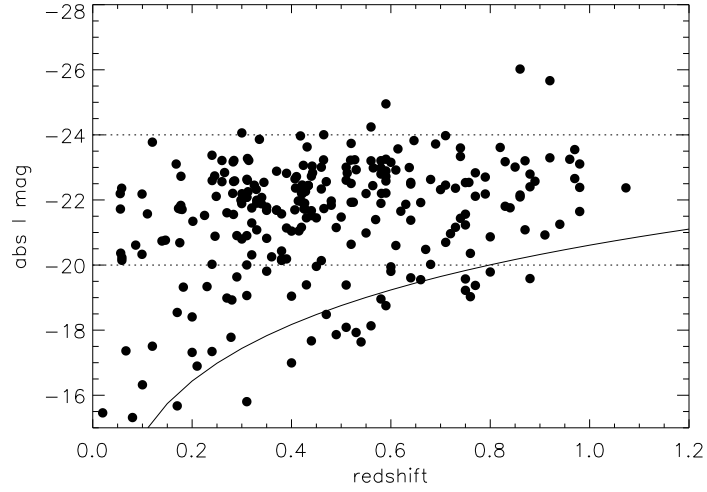


Fig. 18.— Absolute I band magnitude versus redshift for the 266 radio sources with redshift information. The solid line approximates the limit of the optical survey ($I = 23.5$). The dotted lines show the range in magnitude which encompasses about 80% of the radio sources.

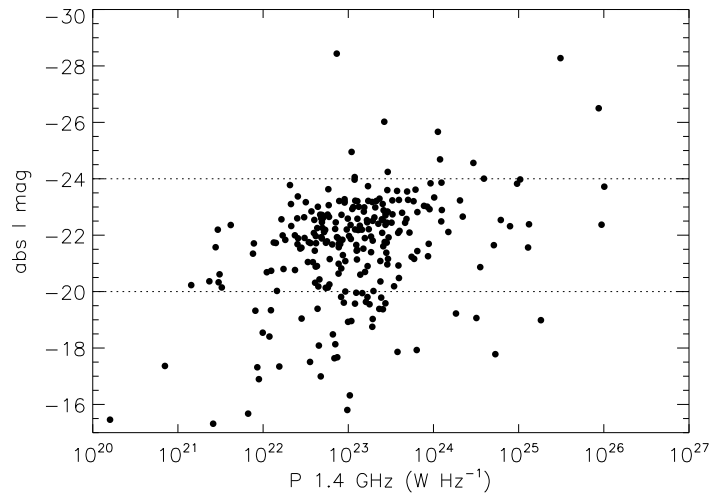


Fig. 19.— Absolute I band magnitude versus radio power, P 1.4 GHz, for the 266 radio sources with redshift information. The dotted lines show the range in magnitude which encompasses about 80% of the radio sources.

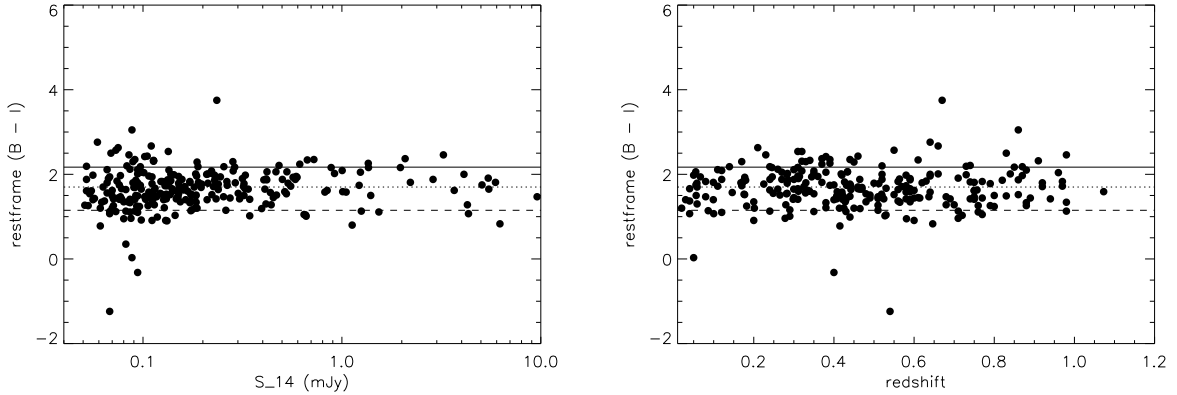


Fig. 20.— Left Panel: The 1.4 GHz flux density versus restframe (B - I) color for the 266 radio sources with redshift information. The solid, dotted and dashed lines show the restframe colors of a E/S0, Sbc and Irr galaxy (Coleman et al. 1980), respectively. Right Panel: Redshift versus restframe (B - I) color for the 266 radio sources with redshift information. The lines are as for the left panel.

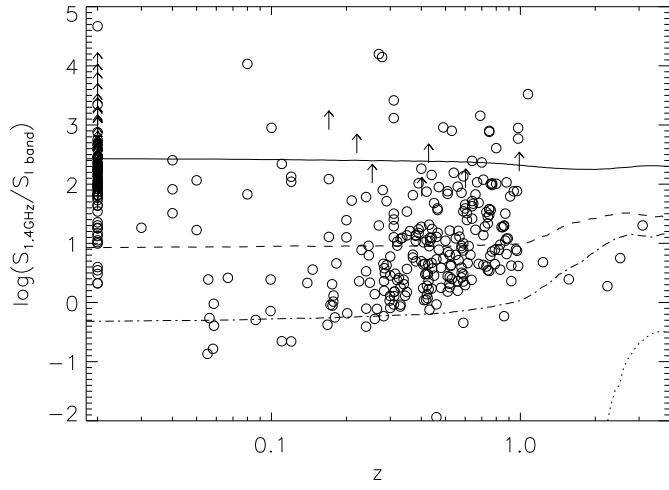


Fig. 21.— The radio-to-optical flux density ratio for sources in the ATHDFS, plotted against redshift. The arrows mark lower limits of ATHDFS sources not detected in the I band imaging. Sources without a redshift are plotted at $z = 0.02$. The tracks for a radio-loud (black solid line) and radio-quiet (dotted line) from Elvis et al. (1994) are plotted for comparison. Also plotted are the ratios from prototypical starbursts Arp220 (dashed line) and M82 (dot-dashed line).

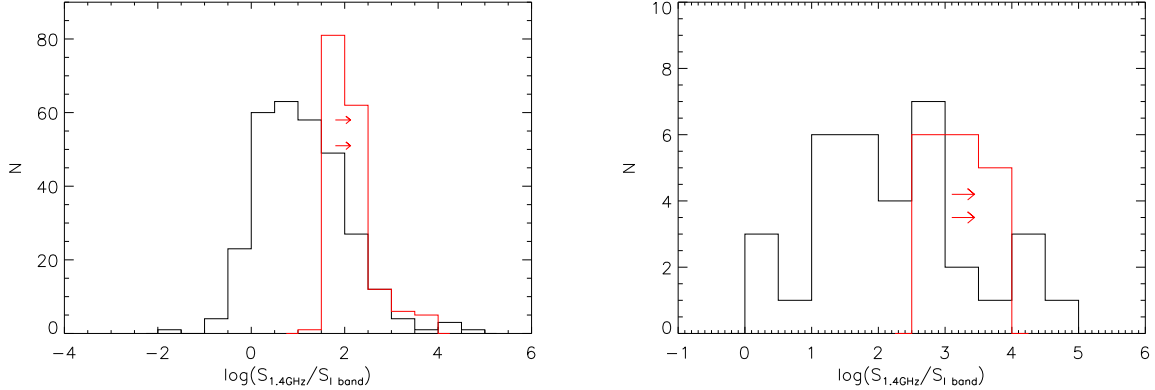


Fig. 22.— The radio-to-optical ratio (R_I) distribution of the ATHDFS sources with CTIO I band counterparts (black solid line). The lower limit of R_I for sources not detected in I band are determined using the nominal CTIO I band limit of 23.5 mag. These lower limits are shown as the red histogram. LEFT: full ATHDFS sample. RIGHT: radio-bright ($S_{1.4\text{GHz}} > 1 \text{ mJy}$) sample.

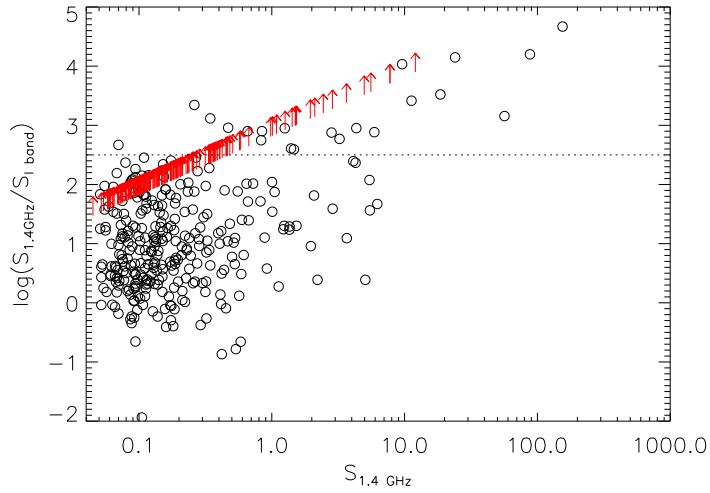


Fig. 23.— The radio-to-optical ratio (R_I) plotted against 1.4 GHz flux density. The dotted line marks our radio-loud criterion of $R_I > 2.5$. The bright ($S_{1.4\text{GHz}} > 1 \text{ mJy}$) radio sources have higher ratios than the faint sub-mJy radio sources, which have intermediate radio-to-optical ratios of $0 < R_I < 1$. There is a sizeable number of radio sources at the 0.1 mJy level with $R_I \gtrsim 2$, as indicated by the radio sources not detected in the I band imaging (arrows), and some of these may be radio-loud AGN.

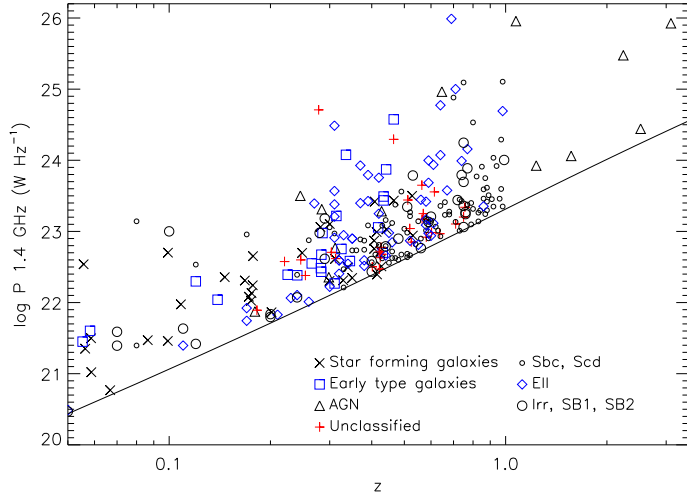


Fig. 24.— The 1.4 GHz luminosity (W Hz^{-1}) of all our radio sources that have redshifts, as a function of redshift. Symbols are as shown in the legend. The left column of the legend is for sources with 2dF spectroscopic redshifts, and the right column for sources with photometric redshifts. The solid line marks the detection limit of 0.050 mJy.

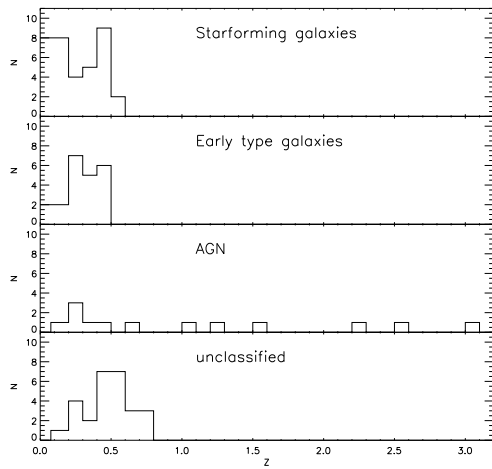


Fig. 25.— The redshift distribution of our radio sources with 2dF spectra. Different spectral classes are drawn separately. From top to bottom: starforming galaxies, early type galaxies, AGN, and unclassified. See text for description of classes.

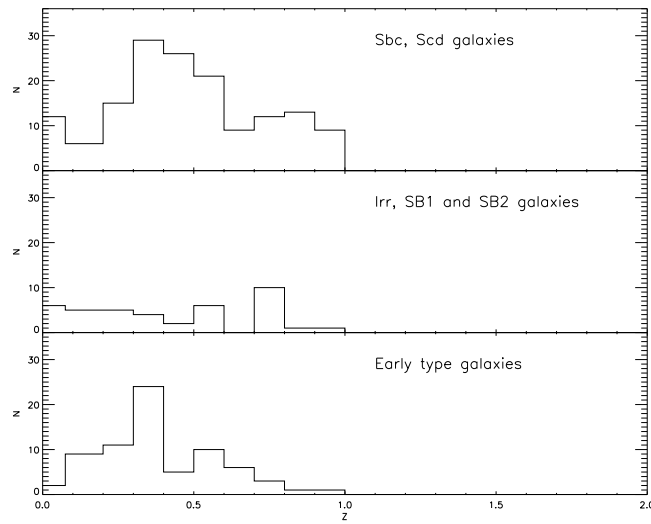


Fig. 26.— The redshift distribution of our radio sources with photometric redshifts. Samples with different best fit templates are drawn separately. From top to bottom: late type galaxies (Sbc and Scd), starbursts/irregulars, and early type galaxies. See text for description of classes.

Table 1. CTIO properties of the catalogued ATHDFS sources.

Table 1—Continued

ATHDFS name	CTIO flag	CTIO ID	U mag	U rms error	B mag	B rms error	V mag	V rms error	R mag	R rms error	I mag	I rms error	CTIO phot z	CTIO phot z uncertainty
ATHDFS_J223413.1-604909	YES	9829	19.31	0.02	19.68	0.01	18.68	0.01	18.13	0.01	17.51	0.02	0.19	0.11
ATHDFS_J223502.1-604858	NO
ATHDFS_J223107.4-604855	YES	9250	26.25	8.03	25.67	1.84	24.14	0.90	23.18	0.60	21.86	0.86	0.00	0.00
ATHDFS_J223400.5-604903A	YES	9201	22.77	0.23	24.21	0.32	23.72	0.42	23.50	0.53	22.82	1.30	0.00	0.00
ATHDFS_J223400.5-604903B	YES	62540	24.33	0.66	25.22	0.52	24.75	0.72	24.02	0.54	23.31	1.20	0.00	0.00
ATHDFS_J223359.4-604901	YES	62540	24.33	0.66	25.22	0.52	24.75	0.72	24.02	0.54	23.31	1.20	0.00	0.00
ATHDFS_J223417.0-604857	NO
ATHDFS_J223543.9-604838	YES	10095	22.38	0.24	22.18	0.08	20.69	0.04	19.41	0.02	18.50	0.04	0.45	0.02
ATHDFS_J223407.5-604847	NO
ATHDFS_J223234.6-604844	YES	9555	25.18	0.76	26.00	0.54	24.70	0.36	23.47	0.16	22.19	0.16	0.00	0.00
ATHDFS_J223447.4-604843	NO
ATHDFS_J223452.0-604834	YES	10103	22.10	0.10	22.05	0.04	20.91	0.03	20.24	0.02	19.47	0.05	0.48	0.20
ATHDFS_J223337.8-604833	YES	10186	22.42	0.16	22.27	0.07	21.25	0.05	20.18	0.03	19.31	0.06	0.67	0.08
ATHDFS_J223146.9-604827	NO
ATHDFS_J223255.7-604823	YES	10223	22.86	0.22	23.47	0.14	22.53	0.12	21.44	0.06	20.36	0.10	0.78	0.09
ATHDFS_J223250.5-604814	YES	10508	21.79	0.12	22.05	0.06	21.46	0.06	20.52	0.04	19.61	0.08	0.74	0.37
ATHDFS_J223109.5-604810	YES	62785	23.36	0.44	24.21	0.36	24.03	0.60	24.19	1.06	22.68	1.24	0.00	0.00
ATHDFS_J223359.7-604806	NO
ATHDFS_J223243.0-604758	YES	10708	21.50	0.06	21.93	0.03	21.34	0.03	20.58	0.02	19.95	0.06	0.60	0.19
ATHDFS_J223414.7-604753	YES	11505	19.54	0.02	19.62	0.01	18.55	0.01	17.95	0.01	17.27	0.01	0.03	0.05
ATHDFS_J223217.6-604751	YES	10719	22.52	0.10	23.03	0.06	22.70	0.08	22.21	0.08	21.51	0.16	1.24	0.09
ATHDFS_J223417.5-604749	YES	11211	19.80	0.02	20.11	0.01	19.33	0.01	18.92	0.01	18.38	0.03	0.04	0.05
ATHDFS_J223226.8-604745	YES	10922	24.23	0.43	24.55	0.24	23.46	0.16	22.26	0.09	21.32	0.14	0.71	0.12
ATHDFS_J223254.0-604736	NO
ATHDFS_J223340.2-604730	NO
ATHDFS_J223141.7-604725	NO
ATHDFS_J223353.3-604723	YES	11347	22.93	0.19	23.83	0.18	23.39	0.26	22.79	0.22	21.57	0.29	2.05	0.01
ATHDFS_J223527.5-604714	NO
ATHDFS_J223444.0-604710	NO
ATHDFS_J223108.1-604706	NO
ATHDFS_J223315.8-604707	YES	11750	24.30	0.60	26.17	1.16	23.76	0.24	22.50	0.11	21.50	0.19	0.00	0.00
ATHDFS_J223420.4-604658	NO
ATHDFS_J223527.8-604639A	YES	63579	21.69	0.18	21.43	0.06	20.08	0.03	18.93	0.02	18.01	0.04	0.00	0.00
ATHDFS_J223527.8-604639B	NO
ATHDFS_J223231.6-604654	YES	11995	22.78	0.15	23.44	0.10	22.60	0.10	21.63	0.06	20.46	0.07	0.86	0.07
ATHDFS_J223254.0-604650	YES	77236	23.08	0.31	23.18	0.12	22.21	0.10	21.29	0.06	20.28	0.11	0.00	0.00
ATHDFS_J223147.2-604647	NO
ATHDFS_J223305.3-604647	YES	12766	21.82	0.14	21.20	0.03	19.73	0.02	18.72	0.01	17.92	0.03	0.34	0.04
ATHDFS_J223118.9-604644	YES	12102	22.92	0.18	23.53	0.10	23.03	0.14	22.26	0.09	21.10	0.15	1.15	0.06
ATHDFS_J223333.2-604642	YES	12681	21.46	0.06	21.10	0.02	19.82	0.01	19.03	0.01	18.26	0.02	0.23	0.14
ATHDFS_J223300.3-604640	YES	12226	23.46	0.27	24.29	0.21	24.36	0.47	24.31	0.60	0.00	0.00
ATHDFS_J223228.5-604642	YES	12390	22.18	0.10	22.43	0.06	21.67	0.06	20.64	0.04	19.69	0.06	0.74	0.05
ATHDFS_J223358.8-604632	YES	14668	19.07	0.02	19.19	0.01	18.16	0.01	17.57	0.01	16.86	0.01	0.03	0.05
ATHDFS_J223312.3-604630	NO
ATHDFS_J223330.4-604624	YES	13047	23.75	0.64	22.74	0.14	21.21	0.06	20.03	0.04	19.09	0.07	0.45	0.05
ATHDFS_J223343.7-604603	YES	13093	23.94	0.76	24.51	0.63	23.37	0.41	22.99	0.53	21.42	0.53	0.00	0.00
ATHDFS_J223310.2-604601	YES	13062	26.01	1.29	26.26	0.61	25.21	0.51	24.36	0.30	23.44	0.45	0.00	0.00
ATHDFS_J223258.6-604548	NO
ATHDFS_J223329.6-604537	NO
ATHDFS_J223408.1-604534	NO
ATHDFS_J223342.9-604524	YES	15763	20.42	0.03	20.41	0.02	19.06	0.01	18.33	0.01	17.61	0.02	0.16	0.11
ATHDFS_J223324.0-604516	YES	14909	22.95	0.25	23.12	0.16	21.82	0.08	20.64	0.06	19.72	0.09	0.42	0.07
ATHDFS_J223320.1-604457	YES	14865	26.04	0.81	27.05	0.78	25.75	0.40	25.25	0.40	24.90	0.89	0.00	0.00
ATHDFS_J223343.3-604452	YES	15446	19.21	0.01	19.77	0.01	19.37	0.01	19.15	0.01	18.74	0.02	1.70	0.46
ATHDFS_J223121.4-604448	NO
ATHDFS_J223311.5-604449	YES	15226	23.40	0.22	23.90	0.14	23.49	0.19	23.02	0.19	22.11	0.31	1.06	0.09
ATHDFS_J223319.1-604428	YES	16000	19.26	0.01	19.67	0.01	19.39	0.01	18.92	0.01	18.14	0.01	1.24	0.07
ATHDFS_J223210.3-604433	YES	15892	23.11	0.29	23.55	0.24	22.27	0.12	20.85	0.07	19.46	0.07	0.71	0.36
ATHDFS_J223349.0-604435	YES	15617	24.15	0.41	24.14	0.19	23.17	0.13	21.87	0.07	20.86	0.11	0.48	0.10
ATHDFS_J223356.9-604438	NO

35

Table 1—Continued

ATHDFS name	CTIO flag	CTIO ID	U mag	U rms error	B mag	B rms error	V mag	V rms error	R mag	R rms error	I mag	I rms error	CTIO phot z	CTIO phot z uncertainty
ATHDFS_J223244.1-604437	YES	15346	23.56	0.24	24.92	0.33	24.12	0.26	23.82	0.36	23.66	1.16	0.32	0.16
ATHDFS_J223147.2-604415	YES	16415	23.89	0.64	23.18	0.17	21.49	0.06	20.11	0.04	19.14	0.06	0.48	0.02
ATHDFS_J223236.3-604416	YES	15866	27.61	4.92	26.91	1.08	25.48	0.49	24.78	0.40	23.79	0.54	0.00	0.00
ATHDFS_J223255.2-604415	NO
ATHDFS_J223422.4-604412	YES	16135	23.26	0.30	23.65	0.19	22.86	0.16	22.02	0.13	20.79	0.16	0.89	0.08
ATHDFS_J223226.8-604408	YES	16159	24.62	0.64	24.48	0.26	23.65	0.20	22.70	0.15	21.37	0.16	0.86	0.17
ATHDFS_J223313.9-604359	YES	17040	19.46	0.01	19.67	0.01	18.79	0.01	18.30	0.01	17.71	0.02	1.99	0.30
ATHDFS_J223255.6-604400	NO
ATHDFS_J223101.3-604351	YES	16350	26.99	5.97	24.49	0.25	24.05	0.30	23.69	0.35	22.73	0.60	1.49	2.04
ATHDFS_J223319.1-604348	YES	64451	25.10	0.39	25.82	0.29	25.61	0.41	25.93	0.88	0.00	0.00
ATHDFS_J223147.4-604338	YES	17120	20.60	0.03	21.08	0.02	20.65	0.03	20.04	0.03	19.41	0.07	0.60	0.11
ATHDFS_J223216.2-604337	YES	17692	18.28	0.01	18.40	0.00	17.89	0.00	17.53	0.00	17.11	0.01	0.01	0.07
ATHDFS_J223439.7-604337	NO
ATHDFS_J223534.3-604328	YES	16988	24.22	0.27	25.11	0.22	24.66	0.29	24.14	0.25	23.66	0.56	0.64	0.14
ATHDFS_J223250.6-604336	YES	16978	23.93	0.34	24.05	0.16	23.37	0.17	22.62	0.13	21.55	0.18	1.11	0.18
ATHDFS_J223252.2-604326	YES	18162	19.34	0.01	19.57	0.01	18.72	0.01	18.25	0.01	17.62	0.02	1.87	0.32
ATHDFS_J223330.4-604332	NO
ATHDFS_J223355.6-604315	YES	64709	24.40	0.46	23.85	0.45	23.17	0.50	22.15	0.72	0.00	0.00
ATHDFS_J223440.4-604309	YES	18005	20.50	0.02	20.84	0.02	19.77	0.01	19.12	0.01	18.47	0.02	0.34	0.17
ATHDFS_J223430.8-604310	YES	18194	21.05	0.05	21.41	0.03	20.33	0.02	19.68	0.02	19.04	0.05	0.34	0.17
ATHDFS_J223240.2-604306	YES	18233	20.22	0.02	20.74	0.01	19.90	0.01	19.27	0.01	18.63	0.02	0.51	0.14
ATHDFS_J223207.9-604305	YES	17752	22.56	0.11	22.92	0.07	22.12	0.06	21.23	0.04	20.28	0.07	0.74	0.13
ATHDFS_J223427.3-604258	NO
ATHDFS_J223130.4-604232	YES	18511	28.96	16.49	25.55	1.28	23.58	0.35	22.60	0.55	0.00	0.00
ATHDFS_J223425.8-604232	NO
ATHDFS_J223239.0-604230	YES	18609	25.31	1.12	24.40	0.22	23.45	0.16	22.69	0.13	22.14	0.29	0.03	0.04
ATHDFS_J223312.4-604227	YES	18851	22.69	0.13	22.88	0.07	21.86	0.05	20.97	0.04	20.26	0.07	0.57	0.07
ATHDFS_J223437.2-604214	YES	19594	22.44	0.21	22.43	0.11	20.99	0.05	19.67	0.03	18.78	0.05	0.45	0.03
ATHDFS_J223508.5-604217	NO
ATHDFS_J223338.8-604216	YES	20683	19.62	0.03	20.13	0.02	19.34	0.02	18.91	0.03	18.15	0.05	1.65	0.18
ATHDFS_J223523.6-604207	YES	19238	24.90	0.73	25.19	0.42	23.60	0.17	22.34	0.09	21.34	0.13	0.48	0.04
ATHDFS_J223135.8-604207	YES	19624	23.06	0.32	22.89	0.12	21.29	0.05	20.12	0.03	19.26	0.06	0.40	0.03
ATHDFS_J223359.8-604155	YES	22915	16.70	0.00	16.56	0.00	15.79	0.00	15.26	0.00	14.67	0.00	0.10	0.06
ATHDFS_J223255.4-604151	YES	19803	20.27	0.02	21.03	0.01	20.45	0.01	20.13	0.01	19.85	0.04	0.16	0.15
ATHDFS_J223158.4-604142	YES	19985	23.23	0.20	23.62	0.15	22.74	0.10	21.69	0.07	20.56	0.09	0.82	0.09
ATHDFS_J223339.5-604131	YES	20376	21.86	0.06	21.82	0.03	20.56	0.01	19.88	0.01	19.16	0.02	0.00	0.00
ATHDFS_J223224.5-604113	YES	20664	23.84	0.40	24.93	0.47	23.13	0.17	21.62	0.07	20.40	0.08	0.60	0.07
ATHDFS_J223206.5-604102	NO
ATHDFS_J223448.3-604042	YES	21863	20.14	0.02	20.20	0.01	19.38	0.01	18.88	0.01	18.24	0.02	0.11	0.09
ATHDFS_J223430.1-604043	YES	21416	21.82	0.10	22.13	0.05	21.27	0.05	20.25	0.03	19.52	0.06	0.60	0.06
ATHDFS_J223251.1-604042	NO
ATHDFS_J223514.4-604024	NO
ATHDFS_J223348.2-604026	NO
ATHDFS_J223429.8-604020	NO
ATHDFS_J223417.8-604009	NO
ATHDFS_J223337.5-604006	YES	22318	21.27	0.05	21.80	0.04	20.84	0.03	20.21	0.03	19.71	0.06	0.40	0.05
ATHDFS_J223412.2-603957	YES	22415	24.04	1.21	23.85	0.39	23.48	0.56	22.35	0.32	21.20	0.52	0.00	0.00
ATHDFS_J223438.0-603951	YES	22360	24.86	1.14	24.95	0.47	23.16	0.18	21.80	0.07	21.03	0.16	0.42	0.05
ATHDFS_J223343.9-603953	NO
ATHDFS_J223047.9-603933	YES	22586	22.88	0.21	23.11	0.09	21.90	0.06	21.01	0.04	20.24	0.09	0.57	0.05
ATHDFS_J223324.7-603934	NO
ATHDFS_J223220.6-603931	YES	23537	21.07	0.08	20.73	0.03	19.20	0.01	18.28	0.01	17.52	0.02	0.30	0.03
ATHDFS_J223529.2-603927	YES	23056	24.10	0.39	22.45	0.17	21.00	0.07	19.84	0.11	0.54	0.25
ATHDFS_J223400.2-603930	YES	23076	21.83	0.12	22.42	0.08	21.71	0.09	20.91	0.07	19.91	0.12	0.71	0.13
ATHDFS_J223207.9-603928	NO
ATHDFS_J223222.7-603924	YES	23175	20.75	0.03	21.26	0.02	20.32	0.02	19.56	0.02	18.96	0.03	0.54	0.06
ATHDFS_J223253.7-603921	YES	22985	23.51	0.41	24.16	0.26	22.93	0.18	21.85	0.09	20.68	0.13	0.54	0.14
ATHDFS_J223331.3-603914	YES	23177	24.95	0.75	24.83	0.27	23.58	0.17	22.31	0.08	21.28	0.12	0.48	0.07
ATHDFS_J223123.1-603903	YES	23227	26.93	5.15	24.53	0.19	24.15	0.27	23.34	0.17	22.87	0.48	0.16	0.34
ATHDFS_J223258.7-603903	NO

Table 1—Continued

ATHDFS name	CTIO flag	CTIO ID	U mag	U rms error	B mag	B rms error	V mag	V rms error	R mag	R rms error	I mag	I rms error	CTIO phot z	CTIO phot z uncertainty
ATHDFS_J223245.6-603857	YES	23411	24.43	0.46	25.50	0.41	25.45	0.77	24.60	0.46	23.39	0.64	0.00	0.00
ATHDFS_J223205.9-603857	NO
ATHDFS_J223144.4-603858	YES	23788	21.83	0.13	21.52	0.04	20.02	0.02	19.01	0.01	18.29	0.03	0.32	0.02
ATHDFS_J223153.7-603853	YES	23604	21.44	0.07	21.98	0.04	21.53	0.05	20.82	0.04	20.08	0.10	0.89	0.22
ATHDFS_J223450.4-603844	YES	25648	21.66	0.15	21.32	0.05	19.86	0.03	18.61	0.02	17.75	0.03	0.42	0.02
ATHDFS_J223307.1-603846	YES	23987	22.82	0.25	22.86	0.10	21.97	0.09	20.88	0.05	20.12	0.11	0.64	0.05
ATHDFS_J223457.3-603840	YES	24550	20.84	0.05	21.12	0.03	20.22	0.02	19.24	0.02	18.43	0.03	0.64	0.05
ATHDFS_J223232.3-603842	YES	66389	24.52	1.26	24.34	0.48	22.92	0.26	22.20	0.23	20.85	0.25	0.00	0.00
ATHDFS_J223335.9-603828	YES	66607	21.90	0.09	21.78	0.04	20.77	0.03	19.90	0.02	19.10	0.04	0.00	0.00
ATHDFS_J223505.5-603825	NO
ATHDFS_J223304.6-603835	YES	24126	22.97	0.31	22.91	0.11	21.82	0.08	20.75	0.05	19.77	0.08	0.71	0.11
ATHDFS_J223608.1-603823	NO
ATHDFS_J223432.1-603815	YES	24325	26.58	2.35	25.38	0.25	25.13	0.37	24.69	0.32	23.52	0.43	0.00	0.00
ATHDFS_J223187.7-603818	YES	24269	23.74	0.49	24.02	0.23	23.03	0.18	21.83	0.09	20.96	0.18	0.00	0.00
ATHDFS_J223418.6-603808	NO
ATHDFS_J223442.7-603802	NO
ATHDFS_J223248.2-603805	YES	24623	22.96	0.24	23.24	0.11	22.07	0.08	21.24	0.05	20.49	0.11	0.54	0.06
ATHDFS_J223334.4-603804	YES	24536	24.49	0.41	25.76	0.50	25.09	0.55	24.27	0.37	23.83	0.95	0.54	0.21
ATHDFS_J223436.9-603754	YES	24869	24.16	0.74	24.13	0.26	24.63	0.80	22.79	0.22	21.30	0.25	1.29	0.67
ATHDFS_J223346.9-603753	NO
ATHDFS_J223254.5-603748	YES	25724	20.00	0.03	20.17	0.01	19.11	0.01	18.56	0.01	17.91	0.02	0.21	0.12
ATHDFS_J223350.0-603741	YES	25301	24.33	1.08	24.57	0.68	22.69	0.24	21.00	0.09	19.87	0.13	0.00	0.00
ATHDFS_J223441.6-603740	NO
ATHDFS_J223232.8-603737	YES	25211	25.37	0.60	24.38	0.54	23.05	0.22	21.46	0.19	0.00	0.00
ATHDFS_J223142.5-603737	NO
ATHDFS_J223404.8-603732	YES	25233	23.83	0.35	25.17	0.40	24.28	0.35	23.53	0.24	21.60	0.18	0.00	0.00
ATHDFS_J223503.2-603729	YES	66867	25.04	1.16	25.21	0.55	24.94	0.86	23.64	0.40	22.78	0.67	0.00	0.00
ATHDFS_J223437.7-603726	YES	25557	21.10	0.04	21.48	0.02	20.67	0.02	19.98	0.02	19.41	0.04	0.48	0.08
ATHDFS_J223417.1-603724	YES	26355	20.04	0.03	20.22	0.01	19.04	0.01	18.37	0.01	17.70	0.02	0.07	0.08
ATHDFS_J223341.2-603724	YES	25664	22.52	0.15	22.99	0.11	22.63	0.14	21.80	0.11	20.87	0.20	0.82	0.10
ATHDFS_J223225.6-603717	YES	25818	21.92	0.08	22.24	0.04	21.55	0.05	20.70	0.03	20.12	0.07	0.54	0.06
ATHDFS_J223202.5-603714	YES	25570	25.90	1.08	26.45	0.65	25.87	0.72	24.97	0.39	23.60	0.41	0.00	0.00
ATHDFS_J223226.0-603716	NO
ATHDFS_J223506.5-603700	YES	26042	23.57	0.59	23.86	0.37	23.44	0.47	22.97	0.56	23.75	4.46	0.34	0.29
ATHDFS_J223236.6-603657	YES	26333	22.84	0.25	22.75	0.10	21.47	0.06	20.25	0.03	19.33	0.05	0.42	0.06
ATHDFS_J223400.2-603653	YES	27413	18.09	0.01	18.06	0.00	17.26	0.00	16.68	0.00	16.06	0.01	0.12	0.09
ATHDFS_J223255.8-603652	YES	26231	23.45	0.29	24.12	0.18	23.20	0.16	22.18	0.09	20.82	0.11	0.86	0.18
ATHDFS_J223343.7-603651	YES	78036	24.61	0.36	26.82	0.97	26.10	1.01	26.11	1.42	25.51	3.05	0.00	0.00
ATHDFS_J223404.3-603638	YES	26898	24.40	1.30	23.78	0.28	23.25	0.35	21.55	0.11	20.58	0.22	0.48	0.13
ATHDFS_J223154.1-603636	NO
ATHDFS_J223605.7-603631	NO
ATHDFS_J223406.7-603637	YES	27011	19.35	0.01	19.45	0.01	18.80	0.01	18.34	0.01	17.83	0.02	0.01	0.05
ATHDFS_J223054.4-603631	NO
ATHDFS_J223439.9-603629	NO
ATHDFS_J223341.9-603634	YES	67204	27.65	8.70	25.35	0.47	24.79	0.56	25.10	1.12	23.86	1.42	0.00	0.00
ATHDFS_J223451.7-603632	YES	26969	20.81	0.04	21.15	0.02	19.96	0.02	19.33	0.01	18.73	0.03	0.32	0.09
ATHDFS_J223429.9-603629	NO
ATHDFS_J223316.5-603627	YES	26828	21.67	0.07	22.20	0.04	21.75	0.06	21.24	0.05	20.68	0.14	0.60	0.13
ATHDFS_J223526.2-603617	YES	27151	22.06	0.14	22.42	0.07	21.16	0.05	20.41	0.04	19.65	0.09	0.51	0.10
ATHDFS_J223518.7-603619	YES	26781	24.75	0.49	25.20	0.25	24.65	0.36	25.04	0.66	23.83	0.81	0.00	0.00
ATHDFS_J223456.2-603619	NO
ATHDFS_J223158.5-603614	YES	27308	21.20	0.04	21.61	0.03	20.65	0.03	19.85	0.02	19.23	0.05	0.51	0.09
ATHDFS_J223410.3-603613	NO
ATHDFS_J223421.8-603603	YES	27512	20.77	0.04	21.23	0.02	20.35	0.02	19.86	0.02	19.31	0.05	2.05	0.08
ATHDFS_J223232.4-603542A	YES	27891	23.48	0.30	23.06	0.10	21.52	0.04	20.24	0.02	19.38	0.04	0.42	0.01
ATHDFS_J223232.4-603542B	YES	27891	23.48	0.30	23.06	0.10	21.52	0.04	20.24	0.02	19.38	0.04	0.42	0.01
ATHDFS_J223104.8-603549	YES	27508	22.78	0.13	23.44	0.11	22.65	0.09	21.60	0.06	20.71	0.12	0.71	0.06
ATHDFS_J223525.7-603544	YES	28923	18.36	0.01	18.27	0.00	17.73	0.00	17.33	0.00	16.85	0.01	0.04	0.05
ATHDFS_J223229.8-603544	NO
ATHDFS_J223422.0-603544	YES	27716	24.33	0.38	24.64	0.18	24.09	0.20	23.88	0.23	23.77	0.94	2.17	0.31

Table 1—Continued

ATHDFS name	CTIO flag	CTIO ID	U mag	U rms error	B mag	B rms error	V mag	V rms error	R mag	R rms error	I mag	I rms error	CTIO phot z	CTIO phot z uncertainty
ATHDFS_J223224.0-603537	YES	27764	26.70	1.60	25.77	1.15	24.95	0.90	0.00	0.00
ATHDFS_J223253.0-603539	YES	27740	25.28	0.70	25.91	0.48	24.99	0.42	24.15	0.27	23.19	0.51	0.74	0.16
ATHDFS_J223459.4-603535	NO
ATHDFS_J223245.3-603537	YES	27774	25.87	1.23	26.02	0.55	25.47	0.63	24.62	0.45	23.77	0.92	0.00	0.00
ATHDFS_J223046.1-603525	YES	28396	21.21	0.05	21.33	0.03	20.29	0.02	19.38	0.02	18.64	0.03	0.57	0.06
ATHDFS_J223345.5-603532	YES	27950	24.87	0.47	25.15	1.00	23.83	0.54	22.13	0.48	0.00	0.00
ATHDFS_J223338.8-603523	YES	28580	21.65	0.06	21.41	0.02	20.04	0.01	19.29	0.01	18.61	0.02	0.16	0.10
ATHDFS_J223205.3-603519	YES	29715	20.23	0.03	20.26	0.02	18.91	0.01	18.17	0.01	17.49	0.02	0.45	0.08
ATHDFS_J223223.7-603520	NO
ATHDFS_J223344.9-603515	YES	29000	20.28	0.02	20.71	0.02	19.97	0.02	19.25	0.02	18.69	0.04	0.51	0.12
ATHDFS_J223248.8-603509	YES	78160	23.03	0.21	23.21	0.09	22.36	0.07	21.45	0.05	20.55	0.10	0.00	0.00
ATHDFS_J223536.3-603506	YES	28872	22.81	0.25	23.83	0.26	22.81	0.20	21.96	0.15	20.68	0.21	0.89	0.15
ATHDFS_J223410.1-603510	NO
ATHDFS_J223459.5-603502	YES	28888	23.07	0.25	23.55	0.15	22.34	0.10	21.34	0.06	20.61	0.14	0.57	0.04
ATHDFS_J223350.5-603503	YES	28687	26.73	4.97	26.86	2.62	26.25	2.53	24.59	0.97	23.08	0.90	0.00	0.00
ATHDFS_J223229.2-603459A	NO
ATHDFS_J223229.2-603459B	NO
ATHDFS_J223341.5-603454	YES	29243	21.54	0.08	21.72	0.04	20.85	0.03	19.83	0.02	19.02	0.04	0.64	0.05
ATHDFS_J223438.6-603450	YES	30870	20.45	0.04	20.21	0.02	18.96	0.01	17.99	0.01	17.27	0.02	0.30	0.06
ATHDFS_J223103.2-603453	YES	29001	23.97	0.34	23.29	0.08	21.79	0.04	20.65	0.02	19.43	0.03	0.57	0.08
ATHDFS_J223116.4-603452	YES	67850	24.84	0.59	25.40	0.40	25.49	0.81	24.21	0.39	22.56	0.34	0.00	0.00
ATHDFS_J223431.8-603454	YES	28929	25.73	2.84	24.99	0.55	24.90	0.97	23.99	0.67	23.12	1.25	0.00	0.00
ATHDFS_J223425.0-603452	YES	67937	22.08	0.09	22.97	0.07	22.46	0.09	22.00	0.09	21.25	0.18	0.00	0.00
ATHDFS_J223212.3-603448	YES	29588	21.77	0.07	21.91	0.04	21.06	0.03	20.65	0.04	20.18	0.09	0.08	0.03
ATHDFS_J223307.1-603448	NO
ATHDFS_J223207.4-603445	YES	29564	23.83	0.44	23.36	0.14	22.00	0.07	20.87	0.05	20.04	0.08	0.37	0.04
ATHDFS_J223243.3-603443	YES	29735	21.37	0.06	21.67	0.04	20.55	0.02	19.60	0.02	18.87	0.05	0.57	0.02
ATHDFS_J223410.6-603437	NO
ATHDFS_J223442.8-603433	YES	29755	21.99	0.09	22.02	0.05	21.27	0.04	20.61	0.04	19.91	0.08	0.57	0.20
ATHDFS_J223216.6-603434	YES	29597	22.90	0.19	23.71	0.19	23.09	0.18	22.34	0.17	21.28	0.24	1.15	0.14
ATHDFS_J223539.3-603424	YES	78212	23.03	0.26	23.77	0.20	22.80	0.17	21.78	0.10	20.37	0.12	0.00	0.00
ATHDFS_J223153.2-603422	YES	29880	24.50	0.63	24.89	0.42	23.61	0.22	22.30	0.12	21.43	0.23	0.42	0.06
ATHDFS_J223401.0-603424	YES	68104	21.87	0.05	21.90	0.02	20.56	0.01	19.83	0.01	19.14	0.02	0.00	0.00
ATHDFS_J223245.5-603419	YES	30363	23.22	0.29	23.07	0.12	21.95	0.08	21.10	0.06	20.33	0.14	0.54	0.10
ATHDFS_J223231.6-603423	NO
ATHDFS_J223055.9-603412	NO
ATHDFS_J223327.6-603414	NO
ATHDFS_J223311.9-603417	YES	29938	24.89	0.65	27.12	2.08	25.34	0.82	23.72	0.27	23.09	0.70	0.42	0.17
ATHDFS_J223434.1-603410	YES	30150	24.19	0.55	25.20	0.51	25.38	0.99	24.14	0.57	23.62	1.45	0.00	0.00
ATHDFS_J223053.2-603402	YES	30207	23.87	0.30	24.43	0.21	24.35	0.36	23.27	0.21	22.23	0.34	1.15	0.25
ATHDFS_J223415.0-603408	YES	30652	21.90	0.10	22.24	0.05	21.35	0.04	20.41	0.03	19.74	0.07	0.57	0.10
ATHDFS_J223529.7-603359	NO
ATHDFS_J223406.6-603401	NO
ATHDFS_J223409.7-603402	YES	30553	22.58	0.17	22.99	0.10	22.45	0.11	21.73	0.09	20.76	0.16	0.78	0.09
ATHDFS_J223512.7-603353	YES	31037	23.58	0.51	23.66	0.31	22.15	0.12	20.83	0.08	19.65	0.10	0.57	0.05
ATHDFS_J223306.0-603350	YES	32354	18.62	0.01	18.73	0.01	17.77	0.00	17.23	0.00	16.58	0.01	0.17	0.09
ATHDFS_J223329.7-603352	YES	30616	24.60	0.49	25.80	0.64	24.67	0.39	25.12	0.96	23.85	1.08	0.00	0.00
ATHDFS_J223258.5-603346	NO
ATHDFS_J223243.4-603352	YES	30896	19.86	0.01	20.31	0.01	20.28	0.01	19.88	0.01	19.45	0.03	1.24	0.22
ATHDFS_J223545.7-603342	NO
ATHDFS_J223318.5-603344	YES	30791	29.55	49.64	26.22	0.96	24.49	0.36	23.59	0.25	22.94	0.58	0.00	0.00
ATHDFS_J223420.9-603336	YES	31164	22.37	0.18	22.96	0.13	22.62	0.17	22.36	0.24	21.74	0.56	1.11	0.22
ATHDFS_J223225.0-603338	YES	31841	20.69	0.03	21.10	0.02	20.01	0.02	19.40	0.02	18.75	0.04	0.27	0.16
ATHDFS_J223513.7-603333	YES	31824	21.15	0.05	21.45	0.03	20.39	0.02	19.61	0.02	18.92	0.04	0.51	0.15
ATHDFS_J223247.6-603337	YES	31450	21.71	0.07	22.02	0.04	21.05	0.03	20.00	0.02	19.16	0.04	0.67	0.03
ATHDFS_J223337.5-603329	YES	32168	16.90	0.00	17.39	0.00	17.16	0.00	16.93	0.00	16.51	0.00	1.34	0.06
ATHDFS_J223253.1-603329	YES	31266	24.55	0.41	24.76	0.20	24.09	0.22	23.30	0.15	22.29	0.24	1.15	0.24
ATHDFS_J223302.8-603323	YES	68484	23.48	0.39	23.50	0.19	23.28	0.30	22.62	0.28	22.31	0.87	0.00	0.00
ATHDFS_J223309.5-603257	NO
ATHDFS_J223327.9-603304A	NO

38

Table 1—Continued

ATHDFS name	CTIO flag	CTIO ID	U mag	U rms error	B mag	B rms error	V mag	V rms error	R mag	R rms error	I mag	I rms error	CTIO phot z	CTIO phot z uncertainty
ATHDFS_J223327.9-603304B	NO
ATHDFS_J223306.2-603307	NO
ATHDFS_J223339.4-603306	NO
ATHDFS_J223121.6-603301	YES	31880	24.19	0.36	24.45	0.19	23.79	0.19	23.12	0.16	21.69	0.18	1.02	0.15
ATHDFS_J223242.6-603258	NO
ATHDFS_J223234.2-603257	YES	32062	26.55	1.70	25.72	0.32	26.04	0.74	24.94	0.41	24.63	1.03	0.00	0.00
ATHDFS_J223308.6-603251	YES	32373	24.24	0.53	24.56	0.32	23.07	0.16	21.77	0.08	20.45	0.09	0.64	0.09
ATHDFS_J223456.8-603251	YES	68728	23.35	0.28	23.81	0.21	23.51	0.27	23.08	0.34	22.17	0.54	0.00	0.00
ATHDFS_J223323.2-603249	NO
ATHDFS_J223209.7-603253	NO
ATHDFS_J223212.9-603234A	YES	32725	23.60	0.20	24.36	0.18	23.63	0.16	22.99	0.14	22.02	0.21	0.74	0.09
ATHDFS_J223212.9-603234B	YES	32725	23.60	0.20	24.36	0.18	23.63	0.16	22.99	0.14	22.02	0.21	0.74	0.09
ATHDFS_J223229.5-603243	YES	68773	22.61	0.13	23.34	0.12	23.10	0.16	22.49	0.16	21.38	0.21	0.00	0.00
ATHDFS_J223509.4-603235	YES	34751	17.36	0.00	17.07	0.00	16.02	0.00	15.49	0.00	14.89	0.00	3.06	0.11
ATHDFS_J223142.5-603238	YES	68852	21.32	0.06	21.47	0.03	20.28	0.02	19.44	0.02	18.62	0.03	0.00	0.00
ATHDFS_J223251.1-603235	NO
ATHDFS_J223317.7-603235	YES	68832	23.52	0.31	23.47	0.14	22.14	0.07	20.83	0.04	19.57	0.05	0.00	0.00
ATHDFS_J223335.3-603234	NO
ATHDFS_J223429.9-603226	YES	32955	28.98	31.29	26.66	1.29	24.69	0.41	24.08	0.34	23.07	0.53	0.00	0.00
ATHDFS_J223331.6-603222	YES	33347	21.51	0.05	22.04	0.04	21.24	0.03	20.55	0.03	19.90	0.06	0.57	0.10
ATHDFS_J223504.4-603221	YES	33873	22.64	0.19	22.68	0.11	21.44	0.06	20.48	0.05	19.79	0.10	0.54	0.05
ATHDFS_J223343.5-603211	YES	33790	21.89	0.08	22.16	0.05	21.10	0.03	20.01	0.02	19.29	0.05	0.60	0.04
ATHDFS_J223302.1-603213	NO
ATHDFS_J223519.4-603157A	YES	33973	21.71	0.09	21.84	0.04	20.70	0.03	19.87	0.02	19.21	0.04	0.51	0.06
ATHDFS_J223519.4-603157B	YES	34076	21.71	0.10	21.93	0.04	20.96	0.03	20.23	0.03	19.64	0.06	0.51	0.08
ATHDFS_J223351.1-603153	YES	33888	21.56	0.06	22.00	0.04	21.26	0.04	20.36	0.03	19.72	0.05	0.57	0.05
ATHDFS_J223113.5-603147	YES	33669	24.50	0.60	25.27	0.41	25.47	0.95	24.56	0.60	23.02	0.61	0.00	0.00
ATHDFS_J223433.9-603150	YES	33726	24.00	0.37	25.14	0.32	25.19	0.59	24.27	0.39	23.04	0.45	0.00	0.00
ATHDFS_J223449.7-603137	YES	34051	23.05	0.17	23.99	0.14	22.85	0.07	21.61	0.04	20.24	0.04	0.67	0.36
ATHDFS_J223303.1-603132	NO
ATHDFS_J223254.4-603131	NO
ATHDFS_J223316.0-603127	YES	34392	23.14	0.26	23.32	0.11	22.10	0.06	21.03	0.04	20.24	0.09	0.60	0.08
ATHDFS_J223548.9-603113	YES	34854	22.11	0.22	22.47	0.11	21.06	0.06	19.73	0.03	18.71	0.06	0.51	0.05
ATHDFS_J223201.4-603118	YES	34558	21.58	0.07	21.40	0.03	20.06	0.02	19.01	0.01	17.73	0.01	0.60	0.14
ATHDFS_J223351.7-603117	YES	34765	22.83	0.19	23.01	0.09	22.33	0.11	21.47	0.07	20.61	0.13	0.67	0.12
ATHDFS_J223504.6-603109	YES	35154	18.73	0.01	18.62	0.00	17.87	0.00	17.35	0.00	16.82	0.01	0.08	0.04
ATHDFS_J223415.5-603108	YES	34566	24.14	0.47	24.17	0.16	24.30	0.35	24.22	0.44	23.29	0.83	1.20	0.60
ATHDFS_J223256.4-603058	NO
ATHDFS_J223350.9-603050	NO
ATHDFS_J223447.4-603050	YES	35065	22.93	0.20	23.42	0.11	23.14	0.16	22.34	0.11	21.46	0.20	0.89	0.11
ATHDFS_J223146.0-603046	NO
ATHDFS_J223345.0-603041	NO
ATHDFS_J223404.0-603037A	YES	35214	24.73	1.30	24.16	0.27	24.21	0.59	23.25	0.35	22.18	0.61	1.29	0.30
ATHDFS_J223404.0-603037B	YES	35546	23.47	0.24	22.66	0.24	21.76	0.16	20.92	0.37	0.48	0.33
ATHDFS_J223445.6-603032	YES	35422	22.19	0.13	22.59	0.07	22.07	0.08	21.47	0.07	20.51	0.12	1.34	0.02
ATHDFS_J223304.8-603031	YES	35585	21.12	0.05	21.44	0.03	20.58	0.02	19.84	0.02	19.20	0.04	0.54	0.07
ATHDFS_J223120.1-603025	YES	35603	20.72	0.05	21.15	0.03	20.11	0.02	19.27	0.01	18.61	0.04	0.51	0.11
ATHDFS_J223357.7-603013	NO
ATHDFS_J223241.4-603025	YES	35743	20.61	0.03	21.01	0.02	20.06	0.01	19.29	0.01	18.64	0.03	0.54	0.09
ATHDFS_J223414.6-603024	NO
ATHDFS_J223404.4-603017	YES	36010	21.81	0.10	21.63	0.03	20.17	0.02	19.34	0.01	18.60	0.02	0.27	0.05
ATHDFS_J223216.6-603016	YES	36058	21.71	0.07	21.54	0.03	20.53	0.02	19.74	0.02	19.07	0.04	0.48	0.15
ATHDFS_J223453.7-603008	YES	36027	23.71	0.63	23.82	0.26	22.68	0.18	21.42	0.09	20.42	0.15	0.45	0.08
ATHDFS_J223303.9-603013	NO
ATHDFS_J223203.6-603007	NO
ATHDFS_J223331.1-603007	NO
ATHDFS_J223430.1-602959	YES	36102	22.86	0.35	23.21	0.17	22.54	0.19	22.04	0.19	21.59	0.59	0.01	0.04
ATHDFS_J223236.5-603000	NO
ATHDFS_J223224.7-603005	YES	35779	24.83	0.35	25.13	0.18	24.98	0.30	24.33	0.24	24.04	0.64	1.44	0.44
ATHDFS_J223516.8-602959	NO

Table 1—Continued

ATHDFS name	CTIO flag	CTIO ID	U mag	U rms error	B mag	B rms error	V mag	V rms error	R mag	R rms error	I mag	I rms error	CTIO phot z	CTIO phot z uncertainty
ATHDFS_J223355.5-602956	NO
ATHDFS_J223058.4-602952	YES	36196	22.14	0.16	22.88	0.12	22.01	0.11	20.89	0.06	19.77	0.10	0.82	0.10
ATHDFS_J223544.3-602950	NO
ATHDFS_J223530.9-602951	YES	36090	24.72	0.81	24.43	0.20	23.99	0.26	23.85	0.31	22.75	0.49	1.20	0.57
ATHDFS_J223534.2-602948	YES	36657	21.27	0.06	21.12	0.02	20.14	0.02	19.55	0.01	18.87	0.03	0.23	0.19
ATHDFS_J223108.1-602946	YES	69671	23.02	0.30	23.11	0.12	21.71	0.07	20.57	0.04	19.57	0.07	0.00	0.00
ATHDFS_J223410.0-602949	NO
ATHDFS_J223253.7-602946	NO
ATHDFS_J22316.8-602934	YES	36602	23.15	0.45	23.48	0.24	22.53	0.20	22.66	0.37	21.05	0.41	0.89	1.71
ATHDFS_J223329.1-602933	YES	69747	24.19	0.76	24.49	0.42	29.62	...	23.91	0.78	25.77	18.10	0.00	0.00
ATHDFS_J223513.7-602930	YES	36658	25.44	1.73	24.45	0.22	23.98	0.30	23.19	0.20	22.43	0.39	1.44	1.10
ATHDFS_J223140.6-602924	NO
ATHDFS_J223454.1-602926	YES	37519	22.04	0.27	22.22	0.13	20.83	0.07	19.46	0.03	18.29	0.05	0.57	0.05
ATHDFS_J223303.0-602927A	NO
ATHDFS_J223303.0-602927B	NO
ATHDFS_J223415.3-602925	YES	37444	18.54	0.01	18.55	0.00	17.54	0.00	16.97	0.00	16.35	0.01	0.21	0.12
ATHDFS_J223149.1-602924	YES	36667	23.78	0.41	24.34	0.23	24.43	0.49	23.82	0.39	22.92	0.75	1.24	0.19
ATHDFS_J223157.5-602919	YES	37122	23.89	0.81	23.88	0.33	22.74	0.23	22.01	0.19	21.02	0.36	0.67	0.24
ATHDFS_J223447.1-602915	YES	37087	25.89	3.81	23.85	0.21	23.02	0.18	21.85	0.09	20.92	0.16	0.42	0.12
ATHDFS_J223407.4-602913	YES	37021	24.40	0.90	24.15	0.24	24.33	0.57	23.88	0.53	24.49	4.19	0.00	0.00
ATHDFS_J223317.7-602916	YES	37003	23.73	0.25	23.74	0.09	23.46	0.13	23.23	0.15	22.64	0.38	1.54	0.25
ATHDFS_J223117.4-602850	NO
ATHDFS_J223515.2-602856	YES	37927	21.59	0.10	21.68	0.04	20.66	0.03	19.68	0.02	18.94	0.04	0.60	0.03
ATHDFS_J223420.1-602901	YES	37309	25.21	1.04	25.68	0.51	24.81	0.45	23.76	0.23	22.49	0.30	0.00	0.00
ATHDFS_J223445.3-602855	YES	37492	24.49	0.82	23.68	0.14	23.73	0.27	23.06	0.21	22.91	0.75	1.54	0.86
ATHDFS_J223431.7-602859	YES	37577	21.78	0.10	22.05	0.04	21.07	0.03	20.34	0.02	19.74	0.06	0.51	0.08
ATHDFS_J223212.1-602858	YES	37782	21.81	0.07	22.03	0.04	21.08	0.03	20.16	0.02	19.43	0.05	0.57	0.08
ATHDFS_J223505.0-602853	YES	37540	25.95	0.87	24.40	0.41	22.70	0.12	21.97	0.25	0.48	0.13
ATHDFS_J223236.2-602855	YES	37478	23.62	0.31	24.27	0.22	23.71	0.29	23.09	0.24	24.17	2.39	0.34	0.27
ATHDFS_J223108.3-602851	NO
ATHDFS_J223307.7-602853	YES	37500	25.21	1.62	24.11	0.21	25.48	1.52	22.72	0.17	24.35	3.40	1.44	2.50
ATHDFS_J223127.7-602849	NO
ATHDFS_J22326.9-602850	YES	37843	20.62	0.02	20.44	0.01	19.98	0.01	19.62	0.01	19.16	0.03	0.02	0.04
ATHDFS_J223330.5-602849	YES	37778	20.78	0.03	21.40	0.02	20.78	0.02	20.41	0.02	20.18	0.06	0.21	0.06
ATHDFS_J223103.5-602830	NO
ATHDFS_J223138.5-602834	YES	37839	23.42	0.31	24.02	0.19	24.22	0.47	23.18	0.25	22.29	0.50	0.00	0.00
ATHDFS_J223307.0-602827	YES	38077	24.31	1.06	24.52	0.49	22.73	0.19	23.14	0.42	0.00	0.00
ATHDFS_J223436.2-602821	YES	70137	22.55	0.35	23.03	0.20	22.75	0.30	21.83	0.21	20.73	0.37	0.00	0.00
ATHDFS_J223329.4-602811	YES	70238	20.74	0.03	21.30	0.02	21.09	0.04	20.50	0.03	19.87	0.07	0.00	0.00
ATHDFS_J223255.9-602810	NO
ATHDFS_J223413.3-602808	YES	38524	23.78	0.29	26.62	1.27	24.34	0.30	23.62	0.21	22.91	0.46	0.00	0.00
ATHDFS_J223427.0-602802	NO
ATHDFS_J223219.7-602802	NO
ATHDFS_J223114.1-602800	YES	38561	18.50	0.01	31.92	...	22.80	0.16	21.69	0.25	0.00	0.00
ATHDFS_J223133.4-602755	YES	39033	22.10	0.12	22.33	0.05	21.25	0.04	20.30	0.03	19.54	0.06	0.60	0.03
ATHDFS_J223240.7-602755	YES	38800	23.17	0.29	23.54	0.15	23.35	0.27	23.34	0.42	22.18	0.61	0.00	0.00
ATHDFS_J223438.4-602747	NO
ATHDFS_J223454.2-602742	NO
ATHDFS_J223443.9-602739A	YES	39667	22.44	0.22	22.27	0.07	20.77	0.04	19.61	0.02	18.84	0.04	0.37	0.01
ATHDFS_J223443.9-602739B	YES	39667	22.44	0.22	22.27	0.07	20.77	0.04	19.61	0.02	18.84	0.04	0.37	0.01
ATHDFS_J223443.9-602739C	YES	39667	22.44	0.22	22.27	0.07	20.77	0.04	19.61	0.02	18.84	0.04	0.37	0.01
ATHDFS_J223136.1-602731	YES	39429	21.64	0.08	21.87	0.04	20.90	0.03	20.08	0.02	19.42	0.05	0.48	0.15
ATHDFS_J223311.5-602725	NO
ATHDFS_J223142.7-602719	YES	39784	22.08	0.13	22.14	0.05	21.10	0.04	20.12	0.02	19.36	0.06	0.60	0.04
ATHDFS_J223153.1-602723	NO
ATHDFS_J223148.6-602722	NO
ATHDFS_J223332.7-602723	YES	39695	21.76	0.08	22.18	0.04	21.60	0.05	20.84	0.04	20.19	0.09	0.64	0.18
ATHDFS_J223241.5-602719	NO
ATHDFS_J223227.6-602719A	YES	39818	22.13	0.15	22.95	0.17	22.50	0.19	22.05	0.26	20.85	0.33	0.98	0.14
ATHDFS_J223227.6-602719B	NO

40

Table 1—Continued

ATHDFS name	CTIO flag	CTIO ID	U mag	U rms error	B mag	B rms error	V mag	V rms error	R mag	R rms error	I mag	I rms error	CTIO phot z	CTIO phot z uncertainty
ATHDFS_J223418.3-602715	NO
ATHDFS_J223244.5-602719	NO
ATHDFS_J223317.1-602714	NO
ATHDFS_J223312.3-602707	S	78952	22.98	0.27	23.94	0.24	22.51	0.13	20.77	0.04	18.01	0.01	0.00	0.00
ATHDFS_J223415.2-602701	NO
ATHDFS_J223257.4-602657	YES	40051	23.85	0.53	23.91	0.20	23.76	0.36	23.25	0.33	21.82	0.39	0.00	0.00
ATHDFS_J223329.0-602657	YES	40061	24.10	0.69	23.79	0.22	25.17	1.60	23.52	0.53	20.38	0.12	0.00	0.00
ATHDFS_J223432.3-602652	YES	40138	26.26	1.95	26.03	0.49	25.59	0.61	24.42	0.27	23.51	0.47	0.00	0.00
ATHDFS_J223259.9-602654	NO
ATHDFS_J223506.2-602647	YES	40414	23.87	0.46	24.07	0.19	23.14	0.17	22.35	0.12	21.49	0.21	0.64	0.17
ATHDFS_J223359.1-602642	NO
ATHDFS_J223342.2-602639	YES	40697	22.76	0.15	23.77	0.18	23.29	0.23	22.50	0.17	22.30	0.62	0.51	0.12
ATHDFS_J223221.4-602629	YES	40967	22.31	0.11	22.60	0.07	22.05	0.07	21.36	0.07	20.29	0.11	1.20	0.04
ATHDFS_J223400.9-602633	YES	41325	22.25	0.20	21.54	0.04	20.20	0.03	19.01	0.01	18.18	0.03	0.37	0.04
ATHDFS_J223212.4-602632	YES	40679	25.09	0.77	25.16	0.36	24.16	0.25	23.06	0.15	21.88	0.20	0.78	0.16
ATHDFS_J223136.2-602627	YES	41222	21.33	0.07	21.77	0.06	20.82	0.05	19.85	0.03	19.12	0.08	0.60	0.06
ATHDFS_J223432.6-602614	YES	41174	23.48	0.29	23.75	0.13	23.56	0.22	23.03	0.18	22.13	0.35	1.15	0.10
ATHDFS_J223335.3-602615	YES	42237	20.62	0.04	20.39	0.02	19.20	0.01	18.48	0.01	17.76	0.02	0.08	0.13
ATHDFS_J223136.9-602610	YES	41580	21.40	0.06	21.66	0.03	20.68	0.03	19.66	0.02	18.95	0.04	0.60	0.04
ATHDFS_J223322.5-602607	NO
ATHDFS_J223442.5-602601	YES	41560	23.35	0.36	24.12	0.34	23.30	0.31	22.62	0.27	22.28	0.85	0.40	0.20
ATHDFS_J223307.2-602556	NO
ATHDFS_J223148.3-602554	YES	41688	21.98	0.08	22.31	0.05	21.50	0.05	20.69	0.03	20.02	0.07	0.57	0.06
ATHDFS_J223357.8-602548	YES	41825	22.41	0.09	22.55	0.04	22.03	0.04	21.54	0.04	21.07	0.10	0.01	0.05
ATHDFS_J223308.8-602540	NO
ATHDFS_J223202.6-602534	NO
ATHDFS_J223222.4-602532	S	79167	22.65	0.24	17.67	0.00	14.47	0.00	14.23	0.00	13.55	0.00	0.00	0.00
ATHDFS_J223432.2-602530	NO
ATHDFS_J223445.7-602523	NO
ATHDFS_J223351.2-602519	YES	42652	22.55	0.11	22.67	0.06	21.79	0.04	20.86	0.03	20.09	0.06	0.60	0.09
ATHDFS_J223141.1-602506	YES	43090	20.00	0.02	20.27	0.01	19.25	0.01	18.71	0.01	18.09	0.02	0.19	0.09
ATHDFS_J223228.9-602507	NO
ATHDFS_J223134.5-602457	YES	43114	22.96	0.23	23.06	0.13	21.94	0.08	20.74	0.05	19.93	0.10	0.37	0.07
ATHDFS_J223306.6-602425	NO
ATHDFS_J223317.1-602427	YES	43898	23.77	0.53	24.70	0.69	22.07	0.10	21.80	0.17	0.00	0.00
ATHDFS_J223444.9-602417	YES	43772	25.76	2.39	25.27	0.62	24.58	0.54	24.44	0.83	23.58	1.40	0.00	0.00
ATHDFS_J223436.8-602426	YES	43650	23.10	0.19	23.09	0.07	22.42	0.06	21.68	0.05	21.03	0.11	0.54	0.14
ATHDFS_J223245.3-602407	YES	43995	...	26.83	1.07	25.83	0.81	24.71	0.44	24.17	0.96	0.00	0.00	
ATHDFS_J223343.4-602348	YES	44829	22.03	0.08	22.44	0.05	21.98	0.06	21.57	0.07	21.09	0.16	0.14	0.14
ATHDFS_J223410.2-602324	NO
ATHDFS_J223146.3-602313	NO
ATHDFS_J223331.6-602307	YES	45826	23.60	0.34	23.66	0.17	22.32	0.08	21.04	0.05	19.79	0.06	0.00	0.00
ATHDFS_J223343.7-602307	NO
ATHDFS_J223358.9-602258	YES	46088	20.74	0.02	20.97	0.01	20.78	0.01	20.75	0.02	20.54	0.06	0.04	0.05
ATHDFS_J223300.5-602225	YES	46891	23.75	0.34	24.09	0.22	23.39	0.23	22.59	0.17	22.08	0.41	0.51	0.09
ATHDFS_J223154.6-602211	YES	47347	22.45	0.13	23.35	0.14	22.46	0.10	21.49	0.08	20.41	0.12	0.82	0.08
ATHDFS_J223353.6-602136	YES	48095	24.63	0.92	26.30	1.66	25.41	1.40	24.17	0.71	22.80	0.74	0.00	0.00
ATHDFS_J223341.1-602054	YES	49047	24.54	0.55	25.07	0.33	24.65	0.47	23.69	0.27	22.53	0.31	1.02	0.09
ATHDFS_J223359.4-602047	NO
ATHDFS_J223431.4-602041	YES	49407	24.28	1.28	23.22	0.17	22.21	0.14	21.07	0.08	20.02	0.14	0.00	0.00
ATHDFS_J223356.6-601949	YES	50950	21.41	0.09	21.21	0.03	19.75	0.02	18.86	0.01	18.13	0.02	0.27	0.04
ATHDFS_J223316.0-601939	YES	50965	24.45	1.35	23.39	0.20	22.16	0.13	20.71	0.06	19.79	0.10	0.45	0.05
ATHDFS_J223334.5-601928	NO

ATHDFS name	F300 magnitude	F300 rms error	F450 magnitude	F450 rms error	F606 magnitude	F606 rms error	F814 magnitude	F814 rms error	morphological information
ATHDFS_J223258.6-603346	27.53	0.68	28.48	0.77	27.05	0.13	25.12	0.04	no info
ATHDFS_J223247.6-603337	22.70	0.02	21.69	0.00	20.55	0.00	19.55	0.00	late type spiral
ATHDFS_J223253.1-603329	25.00	0.07	24.31	0.02	23.69	0.01	22.56	0.00	no info
ATHDFS_J223302.8-603323	25.45	0.19	23.60	0.02	23.36	0.01	22.79	0.01	barred spiral

Table 2: Summary of WFPC2 counterparts.

ATHDFS name	F110 magnitude	F110 rms error	F160 magnitude	F160 rms error	F222 magnitude	F222 rms error	morphological information
ATHDFS_J223253.7-603921	21.20	0.05	19.97	0.02	19.38	0.07	no info

Table 3: Summary of NICMOS counterparts.

ATHDFS name	50ccd magnitude	50ccd rms error	lp magnitude	lp rms error	nuv magnitude	nuv rms error	fuv magnitude	fuv rms error	morphological information
ATHDFS_J223337.5-603329	17.83	0.0	17.48	0.00	-	-	29.13	0.00	bright point source (STIS QSO)
ATHDFS_J223339.4-603306	24.76	0.01	24.46	0.04	41.00	0.00	37.33	0.00	irregular and disturbed, possible merging system

Table 4: Summary of STIS counterparts.

ATHDFS name	flanking field ID	WFPC2 Flanking Observations					
		F606 magnitude	F606 rms error	F814 magnitude	F814 rms error	morphological information	
ATHDFS_J223207.9-603928	WdpVI	26.46	0.21	25.61	0.15	no info	
ATHDFS_J223253.7-603921	W9	-	-	21.12	0.01	possible merging system	
ATHDFS_J223245.6-603857	W9	-	-	23.91	0.04	no info	
ATHDFS_J223248.2-603805	W9	-	-	20.90	0.01	edge-on disk galaxy	
ATHDFS_J223254.5-603748	W9	-	-	18.44	0.00	barred spiral	
ATHDFS_J223202.5-603714	WdpVI	25.86	0.11	24.17	0.04	possible merging system	
ATHDFS_J223253.0-603539	W6	-	-	23.45	0.04	no info	
ATHDFS_J223338.8-603537	W6	-	-	24.04	0.06	no info	
ATHDFS_J223338.8-603523	W8	-	-	18.99	0.00	early type spiral	
ATHDFS_J223344.9-603515	W8	-	-	19.51	0.00	spiral galaxy in merging system	
ATHDFS_J223350.5-603503	W8	-	-	26.24	0.19	no info	
ATHDFS_J223307.1-603448	W3	-	-	24.83	0.08	no info	
ATHDFS_J223243.3-603443	W2	-	-	19.32	0.00	merging system	
ATHDFS_J223241.5-603419	W2	-	-	21.10	0.01	possible merger	
ATHDFS_J223311.9-603417	W3	-	-	23.93	0.05	no info	
ATHDFS_J223306.0-603350	W3	-	-	17.25	0.00	face-on spiral	
ATHDFS_J223243.4-603352	W2	-	-	19.87	0.00	point-like, quasar	
ATHDFS_J223247.6-603337	W2	-	-	19.64	0.01	spiral	
ATHDFS_J223337.5-603329	W8	-	-	17.70	0.00	bright point source (STIS QSO)	
ATHDFS_J223339.4-603306	W8	-	-	24.81	0.10	no info	
ATHDFS_J223308.6-603251	W1	-	-	21.03	0.01	spheroidal	
ATHDFS_J223317.7-603235	W4	-	-	20.83	0.01	spheroidal	
ATHDFS_J223311.6-603222	W7	-	-	20.38	0.01	merging system, triple nuclei	
ATHDFS_J223303.1-603132	W1	-	-	24.05	0.05	no info	
NICMOS Flanking Observations							
ATHDFS name	flanking field ID	F111 magnitude	F111 rms error	F160 magnitude	F160 rms error	morphological information	
ATHDFS_J223250.6-604336	N9	-	-	22.06	0.02	possible merging system	
ATHDFS_J223337.5-604006	N8	-	-	19.66	0.00	merging system	
ATHDFS_J223334.4-603804	N7	-	-	22.30	0.09	no info (at edge of image)	
ATHDFS_J223210.3-604433	dpJH	20.45	0.03	19.83	0.01	no info (at edge of image)	
STIS Flanking Observations							
ATHDFS name	flanking field ID	50ccd magnitude	50ccd rms error			morphological information	
ATHDFS_J223425.0-603452	S8	23.18	0.01			disturbed, merging system	
ATHDFS_J223327.6-603414	S2	28.17	0.18			no info	

Table 5: Summary of HST flanking field counterparts.

ATHDFS name	CTIO I magnitude	HST F812W magnitude	$S_{1.4\text{GHz}}$ (mJy)
ATHDFS_J223207.9-603928	-	25.61	0.098
ATHDFS_J223253.8-603921	20.68	21.12	0.052
ATHDFS_J223245.6-603857	23.39	23.91	0.843
ATHDFS_J223248.2-603805	20.49	20.90	0.076
ATHDFS_J223254.5-603748	17.91	18.44	0.092
ATHDFS_J223202.5-603714	23.60	24.17	0.148
ATHDFS_J223253.0-603539	23.19	23.45	0.090
ATHDFS_J223245.3-603537	23.77	24.04	0.051
ATHDFS_J223338.8-603523	18.61	18.99	0.185
ATHDFS_J223344.9-603515	18.69	19.51	0.344
ATHDFS_J223350.5-603503	23.08	26.24	1.252
ATHDFS_J223307.1-603448	-	24.83	0.103
ATHDFS_J223243.3-603443	18.87	19.32	0.063
ATHDFS_J223245.5-603419	20.33	21.10	0.265
ATHDFS_J223311.9-603417	23.09	23.93	0.059
ATHDFS_J223306.0-603350	16.58	17.25	0.452
ATHDFS_J223258.6-603346	-	25.12	1.010
ATHDFS_J223243.4-603352	19.45	19.87	0.098
ATHDFS_J223247.6-603337	19.16	19.55	0.075
ATHDFS_J223337.5-603329	16.51	17.70	1.126
ATHDFS_J223253.1-603329	22.29	22.56	0.113
ATHDFS_J223303-603324	22.31	22.79	0.051
ATHDFS_J223339.4-603306	-	24.81	0.058
ATHDFS_J223308.6-603251	20.45	21.03	0.821
ATHDFS_J223317.7-603235	19.57	20.83	0.070
ATHDFS_J223331.6-603222	19.90	20.38	0.395
ATHDFS_J223303.1-603132	-	24.05	0.052

Table 6: The I magnitudes of ATHDFS sources in the HST WFPC2 deep and flanking fields. The 8 sources not detected by CTIO and HST are listed separately in Table 7.

ATHDFS name	$S_{1.4\text{GHz}}$ (mJy)	Radio-to-optical Ratio R_I
ATHDFS_J223258.7-603903	0.058	> 2.60
ATHDFS_J223205.9-603857	0.254	> 3.24
ATHDFS_J223327.6-603414	0.456	> 3.50
ATHDFS_J223327.9-603304A	0.221	> 3.18
ATHDFS_J223327.9-603304B	0.059	> 2.61
ATHDFS_J223323.2-603249	0.457	> 3.50
ATHDFS_J223335.3-603234	0.054	> 2.47
ATHDFS_J223302.1-603213	0.063	> 2.64

Table 7: ATHDFS sources in the HST WFPC2 deep and flanking fields which remain undetected to $I \sim 26.0$.

ATHDFS name	LDSS++ number	redshift	spectral type	comments
ATHDFS_J223241.4-603025	216	0.4250	abs	OII, Balmer-, HK, H β +
ATHDFS_J223247.6-603337	196	0.5803	abs	OII,HK,H δ -,G,H γ -
ATHDFS_J223306.0-603350	133	0.1733	sf	H β +,OIII+,Mgb,5268,H α +,NII+,SII+
ATHDFS_J223245.5-603419	204	0.4606	sf	H β +,OIII(4959+5007)+

Table 8: Summary of LDSS++ spectra (Glazebrook et al. 2006) of ATHDFS radio sources.

ATHDFS name	Sawicki & Mallén-Ornelas (2003) ID	redshift	comments
ATHDFS_J223254.5-603748	90549	0.2668	
ATHDFS_J223243.3-603443	20277	0.4233	
ATHDFS_J223245.5-603419	20462	0.4608	
ATHDFS_J223247.6-603337	672	0.5807	
ATHDFS_J223302.8-603323	894	0.4642	

Table 9: Summary of FORS2 spectra (Sawicki & Mallén-Ornelas 2003) of ATHDFS radio sources.

Table 10. Summary of 2dF spectral properties for ATHDFS sources with 2dF redshifts.

ATHDFS name	2dF redshift	2dF quality	spectral type	H β line flux	OIII[5007] line flux	H α line flux	NII[6584] line flux	comments
ATHDFS_J223356.6-601949	0.2856	3	abs	-	-	-	-	OII, HK, G, Mg
ATHDFS_J223358.9-602258	2.519	3	BL	-	-	-	-	La, OIV], CIV and CIII]
ATHDFS_J223134.5-602457	0.5636	2	unc	-	-	-	-	OII, HK
ATHDFS_J223141.1-602506	0.2485	3	sf	1180±230	680±210	-	-	OII, HK, Hb, OIII
ATHDFS_J223136.9-602610	0.5189	2	unc	-	-	-	-	OII, H, K
ATHDFS_J223335.3-602615	0.1726	3	sf	< 70	< 70	3860±230	3200±280	OII, HK, Ha, N2
ATHDFS_J223400.9-602633	0.4314	3	abs	-	-	-	-	H, K, G, Mg
ATHDFS_J223418.3-602715	0.3034	1	unc	-	-	-	-	OII
ATHDFS_J223311.5-602725	0.1084	3	sf	< 130	< 130	9050±470	3470±260	OII, HK, G, weak Hb, weak OIII, Ha, N2, S2
ATHDFS_J223443.9-602739B	0.4415	2	abs	-	-	-	-	HK, G
ATHDFS_J223330.5-602849	0.4149	3	sf	1730±130	6120±280	-	-	OII, Hb, OIII
ATHDFS_J223515.2-602856	0.4424	3	sf	350±90	890±170	-	-	OII, HK, Hb, OIII
ATHDFS_J223431.7-602859	0.4275	3	sf	640±130	< 150	-	-	OII, H, K, Hb
ATHDFS_J223415.3-602925	0.1679	3	sf	< 100	< 100	4870±330	3170±400	OII, HK, G, Hb, OIII, Ha, N2, S2
ATHDFS_J223108.1-602946	0.5646	1	unc	-	-	-	-	OII
ATHDFS_J223534.2-602948	0.1752	3	sf	< 50	< 50	5050±260	1980±160	OII, Mg, Na, Ha, N2
ATHDFS_J223440.4-603017	0.3251	3	abs	-	-	-	-	HK, Hb abs, G, Mg,
ATHDFS_J223120.1-603025	0.4239	2	unc	-	-	-	-	OII, H
ATHDFS_J223304.8-603031	0.4282	3	unc	-	-	-	-	OII, Hb, OIII
ATHDFS_J223504.6-603109	0.0587	3	sf	6250±460	12800±400	35700±800	9730±480	OII, HK, G, Hb, OIII, Ha, N2, S2
ATHDFS_J223519.4-603157A	0.4081	3	sf	2030±220	1510±230	-	-	OII, Hb, OIII
ATHDFS_J223519.4-603157B	0.4067	3	sf	800±80	570±70	-	-	OII, HB, OIII
ATHDFS_J223343.5-603211	0.5302	3	sf	370±110	878±150	-	-	OII, HK, Hb, OIII
ATHDFS_J223504.4-603221	0.4265	1	unc	-	-	-	-	OIII
ATHDFS_J223331.6-603222	0.4652	3	sf	650±120	1150±100	-	-	OII, Hb, OIII
ATHDFS_J223509.4-603235	0.1200	3	abs	-	-	-	-	H, K, Hb, OIII, Mg, Na
ATHDFS_J223142.5-603238	0.3445	2	abs	-	-	-	-	H, K, Mg
ATHDFS_J223337.5-603329	2.238	3	BL	-	-	-	-	STIS QSO z = 2.238
ATHDFS_J223513.7-603333	0.4070	2	sf	810±150	< 150	-	-	OII, HB
ATHDFS_J223225.0-603338	0.2998	2	sf	-	1210±120	-	-	OII, OIII
ATHDFS_J223243.4-603352	1.566	3	BL	-	-	-	-	CIV, CIII] and MgII
ATHDFS_J223401.0-603424	0.2832	2	abs	-	-	-	-	HK, Mg, G
ATHDFS_J223442.8-603433	0.0668	3	sf	680±390	2460±110	1920±140	< 30	OII, Hb, OIII, Ha
ATHDFS_J223212.3-603448	0.1823	2	unc	-	-	-	-	OII, OIII
ATHDFS_J223438.6-603450	0.3354	3	abs	-	-	-	-	HK, G, Hb abs, Mg

Table 10—Continued

ATHDFS name	2dF redshift	2dF quality	spectral type	H β line flux	OIII[5007] line flux	H α line flux	NII[6584] line flux	comments
ATHDFS_J223541.5-603454	0.6142	1	unc	-	-	-	-	OII
ATHDFS_J223344.9-603515	0.5273	3	sf	2510 \pm 230	940 \pm 120	-	-	OII, Hb, OIII
ATHDFS_J223208.3-603519	0.2841	3	sy	600 \pm 160	11700 \pm 400	-	-	OII, HK, OIII
ATHDFS_J223338.8-603523	0.2250	3	abs	-	-	-	-	H, K, G, OIII
ATHDFS_J223046.1-603525	0.3002	3	sf	2200 \pm 210	6250 \pm 260	-	-	OII, Hb, OIII
ATHDFS_J223232.4-603542A	0.4338	2	abs	-	-	-	-	HK, G
ATHDFS_J223232.4-603542B	0.4338	2	abs	-	-	-	-	HK, G
ATHDFS_J223525.7-603544	0.0586	3	sf	3320 \pm 380	5880 \pm 310	19700 \pm 700	4940 \pm 730	OII, Hb, OIII, Ha, N2, S2
ATHDFS_J223104.8-603549	0.5693	1	unc	-	-	-	-	OII
ATHDFS_J223421.8-603603	0.3499	3	sf	3840 \pm 250	2280 \pm 340	-	-	OII, Hb, OIII
ATHDFS_J223158.5-603614	0.4213	2	unc	-	-	-	-	OII, K
ATHDFS_J223451.7-603632	0.3291	3	sf	900 \pm 110	640 \pm 190	-	-	OII, H, K, Hb, OIII
ATHDFS_J223406.7-603637	0.0991	3	sf	3750 \pm 300	3550 \pm 290	21200 \pm 400	7120 \pm 500	OII, HK, Hb, OIII, Na, Ha, N2, S2
ATHDFS_J223400.2-603653	0.0992	3	sf	7070 \pm 480	4560 \pm 410	64600 \pm 820	22700 \pm 560	OII, HK, Hb, OIII, Na, Ha, N2, S2
ATHDFS_J223417.1-603724	0.2403	3	abs	-	-	-	-	OII, HK, G, Mg, some OIII
ATHDFS_J223437.7-603726	0.4137	3	sf	4420 \pm 160	3310 \pm 310	-	-	OII, Hb, OIII
ATHDFS_J223254.5-603748	0.1798	3	sy	840 \pm 190	4500 \pm 260	5420 \pm 210	1820 \pm 220	OII, H, K, Hb, OIII, Ha, N2
ATHDFS_J223418.6-603808	0.4279	3	sy	2010 \pm 140	19400 \pm 200	-	-	OII, Hb, OIII
ATHDFS_J223450.4-603844	0.4180	2	abs	-	-	-	-	K, G
ATHDFS_J223153.7-603853	0.7500	1	unc	-	-	-	-	OII
ATHDFS_J223144.4-603858	0.3102	3	abs	-	-	-	-	H, K, G, Hb, Mg
ATHDFS_J223123.1-603903	0.2782	1	unc	-	-	-	-	OII
ATHDFS_J223222.7-603924	0.4215	2	unc	-	-	-	-	OII, K, G
ATHDFS_J223220.6-603931	0.2825	3	abs	-	-	-	-	HK, G, Na, Mg
ATHDFS_J223337.5-604006	0.425	3	sf	530 \pm 110	1290 \pm 140	-	-	OII, Hb, OIII
ATHDFS_J223448.3-604042	0.1463	3	sf	< 4000	4090 \pm 280	18600 \pm 500	3330 \pm 210	OII, HK, OIII, Ha
ATHDFS_J223255.4-604151	1.233	2	BL	-	-	-	-	MgII, CIII]
ATHDFS_J223359.8-604155	0.0582	3	abs	-	-	-	-	OII, H, K, G, Mg, Ha, N2
ATHDFS_J223437.2-604214	0.4645	2	unc	-	-	-	-	OII, HK
ATHDFS_J223338.8-604216	0.3113	3	sf	5690 \pm 200	8250 \pm 350	-	-	OII, HK, Hb, OIII
ATHDFS_J223312.4-604227	0.5244	1	unc	-	-	-	-	OII
ATHDFS_J223207.9-604305	0.7570	2	unc	-	-	-	-	OII, HK
ATHDFS_J223240.2-604306	0.2982	2	sy	< 2000	11200 \pm 600	-	-	OII, Hb, OIII, HK
ATHDFS_J223430.8-604310	0.3394	2	sf	< 200	740 \pm 180	-	-	OII, OIII
ATHDFS_J223440.4-604309	0.3124	2	unc	-	-	-	-	OII, H, K

Table 10—Continued

ATHDFS name	2dF redshift	2dF quality	spectral type	H β line flux	OIII[5007] line flux	H α line flux	NII[6584] line flux	comments
ATHDFS_J223522.2-604326	0.1772	3	sf	4830±360	2560±1050	5600±490	2300±220	OII, Hb, Ha, N2, HK
ATHDFS_J223126.2-604337	0.0864	3	sf	5500±350	9600±480	27100±500	6660±300	OII, OIII, Hb, Ha, N2, S2
ATHDFS_J223313.9-604359	0.1758	3	sf	1010±130	< 150	7530±270	3300±360	OII, H, K, G, Hb, Ha, N2, S2
ATHDFS_J223319.1-604428	0.6465	2	BL	-	-	-	-	-
ATHDFS_J223121.4-604448	0.6023	1	unc	-	-	-	-	OII
ATHDFS_J223443.3-604452	3.1	2	BL	-	-	-	-	-
ATHDFS_J223342.9-604524	0.2454	3	sy	480±240	7740±350	-	-	OII, OIII, HK, weak Hb
ATHDFS_J223536.8-604632	0.1775	3	sf	3790±480	2170±1400	25900±500	7670±420	Hb, Ha, low OIII, N2, OII
ATHDFS_J223527.8-604639A	0.4649	2	abs	-	-	-	-	H, K
ATHDFS_J223333.2-604642	0.1393	3	abs	-	-	-	-	abs HK, Na
ATHDFS_J223228.5-604642	0.6370	1	unc	-	-	-	-	H, K, G
ATHDFS_J223417.5-604749	0.2015	3	sf	600±130	420±150	-	-	OII, H, K, Hb, OIII, Ha, N2
ATHDFS_J223217.6-604751	0.7103	1	unc	-	-	-	-	OII
ATHDFS_J223243.0-604758	0.5810	2	unc	-	-	-	-	Hb, OIII but lines in red skylines
ATHDFS_J223452.0-604834	0.2461	2	unc	-	-	-	-	OII, no Hb or OIII
ATHDFS_J223337.8-604833	0.5121	1	unc	-	-	-	-	OII
ATHDFS_J223413.1-604909	0.2653	3	abs	-	-	-	-	OII, HK, Hb
ATHDFS_J223226.9-605029	0.4015	1	unc	-	-	-	-	OII
ATHDFS_J223139.6-605039	0.2834	3	abs	-	-	-	-	H, K, G, Hb, Mg
ATHDFS_J223352.5-605210	0.2540	1	unc	-	-	-	-	OII
ATHDFS_J223454.9-605211	0.0557	3	sf	47500±1100	68300±800	317400±2200	100600±1700	OII, Hb, OIII, Ha, N2, S2
ATHDFS_J223145.4-605311	0.3140	3	abs	-	-	-	-	strong HK, Hb abs, Mg, Na
ATHDFS_J223151.1-605328	0.3114	3	sy	1630±420	19500±400	-	-	OII, OIII, Hb, HK, Na
ATHDFS_J223204.8-605414	0.2817	3	sf	1010±200	1060±210	-	-	OII, H, K, Hb, OIII
ATHDFS_J223214.8-605430	1.073	2	BL	-	-	-	-	MgII, OII and CII
ATHDFS_J223316.9-605533	0.0553	3	abs	-	-	-	-	strong abs HK, Hb, Mg, Na
ATHDFS_J223314.6-605543	0.0563	3	sf	3170±140	3970±190	20300±500	3820±130	OII, H, K, Hb, OIII, Ha, N2, S2
ATHDFS_J223303.6-605751	0.2202	2	unc	-	-	-	-	OII, no Hb or OIII

Table 11. Photometric redshifts of ATHDFS radio sources.

ATHDFS name	Teplitz et al. (2001) Redshift	Redshift (this work)	spectral type
ATHDFS_J223316.9-605533	0.17	0.20	Sbc
ATHDFS_J223353.9-605452	0.98	0.75	Sed
ATHDFS_J223214.8-605430	0.27	0.24	Sed
ATHDFS_J223448.4-605417	0.71	0.80	Sed
ATHDFS_J223204.8-605414	0.21	0.33	Sed
ATHDFS_J223230.3-605352	0.82	0.85	Sbc
ATHDFS_J223151.1-605328	0.32	0.25	E/S0
ATHDFS_J223145.4-605311	0.32	0.25	E/S0
ATHDFS_J223453.4-605259	0.74	0.74	E/S0
ATHDFS_J223203.0-605242B	0.34	0.27	E/S0
ATHDFS_J223458.6-605225	0.71	0.71	E/S0
ATHDFS_J223345.4-605227	1.44	0.48	Irr
ATHDFS_J223454.9-605211	1.70	0.18	Sed
ATHDFS_J223241.8-605209	0.10	0.11	E/S0
ATHDFS_J223223.3-605137	0.51	0.37	E/S0
ATHDFS_J223323.8-605141	0.51	0.68	Sed
ATHDFS_J223420.1-605138	0.82	0.84	Sbc
ATHDFS_J223427.0-605132	0.51	0.38	Sed
ATHDFS_J223238.8-605113	0.78	0.88	Sed
ATHDFS_J223139.6-605039	0.25	0.19	E/S0
ATHDFS_J223142.8-605024	0.51	0.33	E/S0
ATHDFS_J223238.5-605018	0.57	0.59	E/S0
ATHDFS_J223411.6-604931	0.02	0.24	Sbc
ATHDFS_J223221.3-604929	0.51	0.52	E/S0
ATHDFS_J223223.6-604923	0.34	0.52	Sbc
ATHDFS_J223301.3-604926	0.42	0.63	Sbc
ATHDFS_J223414.3-604923	0.42	0.32	E/S0
ATHDFS_J223524.8-604918A	0.78	0.74	Sbc
ATHDFS_J223524.8-604918B	-	0.92	Sbc
ATHDFS_J223413.1-604909	0.19	0.31	Sed
ATHDFS_J223107.4-604855	-	0.31	E/S0
ATHDFS_J223400.5-604903B	-	0.77	Irr
ATHDFS_J223359.4-604901	-	0.59	Irr
ATHDFS_J223543.9-604838	0.45	0.37	E/S0
ATHDFS_J223235.6-604844	-	0.61	E/S0
ATHDFS_J223452.0-604834	0.48	0.31	Sbc
ATHDFS_J223337.8-604833	0.67	0.53	Sbc
ATHDFS_J223255.7-604823	0.78	0.77	Sbc
ATHDFS_J223250.5-604814	0.74	0.59	Sed
ATHDFS_J223243.0-604758	0.60	0.71	Sed
ATHDFS_J223414.7-604753	0.03	0.26	Sbc
ATHDFS_J223217.6-604751	1.24	0.22	SB1

Table 11—Continued

ATHDFS name	Teplitz et al. (2001)	Redshift	Redshift (this work)	spectral type
ATHDFS_J223417.5-604749	0.04		0.14	Sed
ATHDFS_J223226.8-604745	0.71		0.64	Sbc
ATHDFS_J223353.3-604723	2.05		-	—
ATHDFS_J223444.0-604710	-		0.-	SB1
ATHDFS_J223315.8-604707	-		0.55	E/S0
ATHDFS_J223527.8-604639A	-		0.31	E/S0
ATHDFS_J223231.6-604654	-		0.92	Sbc
ATHDFS_J223254.0-604650	-		0.59	Sbc
ATHDFS_J223305.3-604647	0.34		0.26	E/S0
ATHDFS_J223118.9-604644	1.15		0.86	Sed
ATHDFS_J223333.2-604642	0.23		0.15	E/S0
ATHDFS_J223228.5-604642	0.74		0.74	Sbc
ATHDFS_J223536.8-604632	0.03		0.25	Sbc
ATHDFS_J223330.4-604624	0.45		0.34	E/S0
ATHDFS_J223310.2-604601	-		0.47	Sbc
ATHDFS_J223342.9-604524	0.16		0.36	Sbc
ATHDFS_J223324.0-604516	0.42		0.32	E/S0
ATHDFS_J223320.1-604457	-		0.31	Sed
ATHDFS_J223443.3-604452	1.70		0.10	SB1
ATHDFS_J223311.5-604449	1.06		0.51	SB2
ATHDFS_J223319.1-604428	1.24		0.74	SB2
ATHDFS_J223210.3-604433	0.71		0.69	E/S0
ATHDFS_J223439.0-604435	0.48		0.66	Sbc
ATHDFS_J223244.1-604437	0.32		0.44	SB1
ATHDFS_J223147.2-604415	0.48		0.44	E/S0
ATHDFS_J223326.3-604416	-		0.17	E/S0
ATHDFS_J223422.4-604412	0.89		-	—
ATHDFS_J223226.8-604408	0.86		0.86	Sbc
ATHDFS_J223313.9-604359	1.99		0.23	Sed
ATHDFS_J223101.3-604351	1.49		0.04	Sbc
ATHDFS_J223147.4-604338	0.60		0.29	SB2
ATHDFS_J223126.2-604337	0.01		-	—
ATHDFS_J223534.3-604328	0.64		0.53	SB1
ATHDFS_J223250.6-604336	1.11		-	—
ATHDFS_J223522.2-604326	1.87		0.21	Sed
ATHDFS_J223440.4-604309	0.34		0.35	Sed
ATHDFS_J223430.8-604310	0.34		0.35	Sed
ATHDFS_J223240.2-604306	0.51		0.33	Sed
ATHDFS_J223207.9-604305	0.74		0.53	Sed
ATHDFS_J223130.4-604232	-		0.67	E/S0
ATHDFS_J223239.0-604230	0.03		0.05	E/S0
ATHDFS_J223312.4-604227	0.57		0.41	Sbc

Table 11—Continued

ATHDFS name	Teplitz et al. (2001) Redshift	Redshift (this work)	spectral type
ATHDFS_J223437.2-604214	0.45	0.37	E/S0
ATHDFS_J223338.8-604216	1.65	0.32	Irr
ATHDFS_J223523.6-604207	0.48	0.39	E/S0
ATHDFS_J223135.8-604207	0.40	0.32	E/S0
ATHDFS_J223359.8-604155	0.10	0.08	Sbc
ATHDFS_J223255.4-604151	0.16	0.18	SB2
ATHDFS_J223158.4-604142	0.82	0.79	Sbc
ATHDFS_J223339.5-604131	-	0.33	Sbc
ATHDFS_J223224.5-604113	0.60	0.64	E/S0
ATHDFS_J223448.3-604042	0.11	0.21	Scd
ATHDFS_J223430.1-604043	0.60	0.51	Sbc
ATHDFS_J223337.5-604006	0.40	0.34	Scd
ATHDFS_J223438.0-603951	0.42	0.38	E/S0
ATHDFS_J223047.9-603933	0.57	0.44	Sbc
ATHDFS_J223220.6-603931	0.30	0.23	E/S0
ATHDFS_J223529.2-603927	0.54	0.58	E/S0
ATHDFS_J223400.2-603930	0.71	0.68	Scd
ATHDFS_J223222.7-603924	0.54	0.43	Scd
ATHDFS_J223253.7-603921	0.54	0.73	Sbc
ATHDFS_J223331.3-603914	0.48	0.38	E/S0
ATHDFS_J223123.1-603903	0.16	0.06	Sbc
ATHDFS_J223245.6-603857	-	0.75	Irr
ATHDFS_J223144.4-603858	0.32	0.26	E/S0
ATHDFS_J223153.7-603853	0.89	0.52	Irr
ATHDFS_J223450.4-603844	0.42	0.34	E/S0
ATHDFS_J223307.1-603846	0.64	0.55	Sbc
ATHDFS_J223457.3-603840	0.64	0.52	Sbc
ATHDFS_J223232.3-603842	-	0.23	E/S0
ATHDFS_J223304.6-603835	0.71	0.59	Sbc
ATHDFS_J223138.7-603818	-	0.62	Sbc
ATHDFS_J223248.2-603805	0.54	0.40	Sbc
ATHDFS_J223334.4-603804	0.54	0.56	Irr
ATHDFS_J223436.9-603754	1.29	0.97	Sbc
ATHDFS_J223254.5-603748	0.21	0.23	Sbc
ATHDFS_J223350.0-603741	-	0.61	E/S0
ATHDFS_J223232.8-603737	-	0.77	E/S0
ATHDFS_J223404.8-603732	-	0.98	Sbc
ATHDFS_J223437.7-603726	0.48	0.37	Scd
ATHDFS_J223417.1-603724	0.07	0.32	Sbc
ATHDFS_J223341.2-603724	0.82	0.88	Scd
ATHDFS_J223225.6-603717	0.54	0.45	Scd
ATHDFS_J223506.5-603700	0.34	0.05	SB2

Table 11—Continued

ATHDFS name	Teplitz et al. (2001)	Redshift	Redshift (this work)	spectral type
ATHDFS_J223400.2-603653	0.12	0.08	Sbc	
ATHDFS_J223525.8-603652	0.86	0.88	Sbc	
ATHDFS_J223404.3-603638	0.48	0.42	E/S0	
ATHDFS_J223406.7-603637	0.01	0.10	Sed	
ATHDFS_J223341.9-603634	-	0.04	Sed	
ATHDFS_J223451.7-603632	0.32	0.29	Sbc	
ATHDFS_J223316.5-603627	0.60	0.29	SB2	
ATHDFS_J223526.2-603617	0.51	0.37	Sbc	
ATHDFS_J223518.7-603619	-	0.12	SB1	
ATHDFS_J223158.5-603614	0.51	0.42	Sed	
ATHDFS_J223421.8-603603	2.05	0.22	Sed	
ATHDFS_J223232.4-603542A	0.42	-	—	
ATHDFS_J223232.4-603542B	0.42	-	—	
ATHDFS_J223104.8-603549	0.71	0.58	Sed	
ATHDFS_J223525.7-603544	0.04	0.06	Sed	
ATHDFS_J223224.0-603537	-	0.17	Sed	
ATHDFS_J223253.0-603539	0.74	0.58	Sed	
ATHDFS_J223245.3-603537	-	0.51	Sed	
ATHDFS_J223046.1-603525	0.57	0.44	Sbc	
ATHDFS_J223338.8-603523	0.16	0.14	E/S0	
ATHDFS_J223208.3-603519	0.45	0.36	Sbc	
ATHDFS_J223344.9-603515	0.51	0.46	Sed	
ATHDFS_J223524.8-603509	-	0.58	Sbc	
ATHDFS_J223536.3-603506	0.89	0.96	Sbc	
ATHDFS_J223549.5-603502	0.57	0.50	Sbc	
ATHDFS_J223350.5-603503	-	0.98	E/S0	
ATHDFS_J223541.5-603454	0.64	0.53	Sbc	
ATHDFS_J223438.6-603450	0.30	0.19	E/S0	
ATHDFS_J223103.2-603453	0.57	0.58	E/S0	
ATHDFS_J223425.0-603452	-	0.72	SB2	
ATHDFS_J223212.3-603448	0.08	0.17	Sed	
ATHDFS_J223207.4-603445	0.37	0.30	E/S0	
ATHDFS_J223243.3-603443	0.57	0.46	Sbc	
ATHDFS_J223442.8-603433	0.57	0.30	Sed	
ATHDFS_J223216.6-603434	1.15	0.83	Sed	
ATHDFS_J223539.3-603424	-	0.87	Sbc	
ATHDFS_J223153.2-603422	0.42	0.35	E/S0	
ATHDFS_J223401.0-603424	-	0.13	E/S0	
ATHDFS_J223245.5-603419	0.54	0.39	Sbc	
ATHDFS_J223311.9-603417	0.42	0.64	Sbc	
ATHDFS_J223434.1-603410	-	0.76	Irr	
ATHDFS_J223053.2-603402	1.15	0.94	Sed	

Table 11—Continued

ATHDFS name	Teplitz et al. (2001)	Redshift	Redshift (this work)	spectral type
ATHDFS_J223415.0-603408	0.57	0.48	Sed	
ATHDFS_J223409.7-603402	0.78	0.79	Sed	
ATHDFS_J223512.7-603353	0.57	0.58	E/S0	
ATHDFS_J223306.0-603350	0.17	0.30	Sed	
ATHDFS_J223329.7-603352	-	0.11	SB1	
ATHDFS_J223243.4-603352	1.24	0.81	SB1	
ATHDFS_J223138.5-603344	-	0.24	E/S0	
ATHDFS_J223420.9-603336	1.11	0.10	SB1	
ATHDFS_J223225.0-603338	0.27	0.35	Sed	
ATHDFS_J223513.7-603333	0.51	0.36	Sbc	
ATHDFS_J223247.6-603337	0.67	0.56	Sbc	
ATHDFS_J223337.5-603329	1.34	-	—	
ATHDFS_J223253.1-603329	1.15	0.60	Sed	
ATHDFS_J223121.6-603301	1.02	-	—	
ATHDFS_J223308.6-603251	0.64	0.64	E/S0	
ATHDFS_J223456.8-603251	-	0.20	SB1	
ATHDFS_J223229.5-603243	-	0.75	Irr	
ATHDFS_J223509.4-603235	3.06	0.22	Sbc	
ATHDFS_J223142.5-603238	-	0.42	Sbc	
ATHDFS_J223317.7-603235	-	0.60	E/S0	
ATHDFS_J223429.9-603226	-	0.21	E/S0	
ATHDFS_J223331.6-603222	0.57	0.42	Sed	
ATHDFS_J223504.4-603221	0.54	0.45	Sbc	
ATHDFS_J223343.5-603211	0.60	0.53	Sbc	
ATHDFS_J223519.4-603157A	0.51	0.38	Sbc	
ATHDFS_J223519.4-603157B	0.51	0.38	Sed	
ATHDFS_J223433.9-603150	-	0.75	Irr	
ATHDFS_J223449.7-603137	0.67	0.83	Sbc	
ATHDFS_J223316.0-603127	0.60	0.52	Sbc	
ATHDFS_J223548.9-603113	0.51	0.39	E/S0	
ATHDFS_J223201.4-603118	0.60	0.59	E/S0	
ATHDFS_J223351.7-603117	0.67	0.49	Sed	
ATHDFS_J223504.6-603109	0.08	0.05	Sbc	
ATHDFS_J223415.5-603108	1.20	-	—	
ATHDFS_J223447.4-603050	0.89	-	—	
ATHDFS_J223404.0-603037A	1.29	-	—	
ATHDFS_J223404.0-603037B	0.48	0.17	E/S0	
ATHDFS_J223445.6-603032	1.34	0.98	Sed	
ATHDFS_J223304.8-603031	0.54	0.40	Sed	
ATHDFS_J223120.1-603025	0.51	0.37	Sbc	
ATHDFS_J223241.4-603025	0.54	0.41	Sed	
ATHDFS_J223440.4-603017	0.27	0.19	E/S0	

Table 11—Continued

ATHDFS name	Teplitz et al. (2001)	Redshift	Redshift (this work)	spectral type
ATHDFS_J223216.6-603016	0.48	0.33	Sbc	
ATHDFS_J223453.7-603008	0.45	0.35	E/S0	
ATHDFS_J223430.1-602959	0.01	0.28	Irr	
ATHDFS_J223224.7-603005	1.44	-	—	
ATHDFS_J223058.4-602952	0.82	0.82	Sbc	
ATHDFS_J223530.9-602951	1.20	-	—	
ATHDFS_J223534.2-602948	0.23	0.21	Sbc	
ATHDFS_J223108.1-602946	-	0.32	E/S0	
ATHDFS_J223316.8-602934	0.89	0.12	Sed	
ATHDFS_J223513.7-602930	1.44	0.08	Sbc	
ATHDFS_J223454.1-602926	0.57	0.56	E/S0	
ATHDFS_J223415.3-602925	0.21	0.21	Sbc	
ATHDFS_J223149.1-602924	1.24	-	—	
ATHDFS_J223157.5-602919	0.67	0.36	Sbc	
ATHDFS_J223447.1-602915	0.42	0.31	E/S0	
ATHDFS_J223317.7-602916	1.54	0.04	Irr	
ATHDFS_J223515.2-602856	0.60	0.47	Sbc	
ATHDFS_J223420.1-602901	-	0.87	Sbc	
ATHDFS_J223445.3-602855	1.54	-	—	
ATHDFS_J223431.7-602859	0.51	0.39	Sed	
ATHDFS_J223212.1-602858	0.57	0.42	Sbc	
ATHDFS_J223505.0-602853	0.48	0.45	E/S0	
ATHDFS_J223236.2-602855	0.34	0.40	SB2	
ATHDFS_J223307.7-602853	1.44	0.54	Sed	
ATHDFS_J223326.9-602850	0.02	0.02	Sed	
ATHDFS_J223330.5-602849	0.21	0.35	SB2	
ATHDFS_J223138.5-602834	-	0.76	Irr	
ATHDFS_J223307.0-602827	-	0.07	SB2	
ATHDFS_J223436.2-602821	-	0.89	Sed	
ATHDFS_J223329.4-602811	-	0.24	SB1	
ATHDFS_J223413.3-602808	-	0.66	Sed	
ATHDFS_J223114.1-602800	-	0.75	Irr	
ATHDFS_J223133.4-602755	0.60	0.46	Sbc	
ATHDFS_J223443.9-602739A	0.37	0.31	E/S0	
ATHDFS_J223443.9-602739B	0.37	0.31	E/S0	
ATHDFS_J223443.9-602739C	0.37	0.31	E/S0	
ATHDFS_J223136.1-602731	0.48	0.35	Sbc	
ATHDFS_J223142.7-602719	0.60	0.47	Sbc	
ATHDFS_J223332.7-602723	0.64	0.71	Sed	
ATHDFS_J223227.6-602719A	0.98	0.74	SB2	
ATHDFS_J223312.3-602707	-	0.86	E/S0	
ATHDFS_J223432.3-602652	-	0.80	Sbc	

Table 11—Continued

ATHDFS name	Teplitz et al. (2001) Redshift	Redshift (this work)	spectral type
ATHDFS_J223506.2-602647	0.64	0.46	Scd
ATHDFS_J223342.2-602639	0.51	0.60	Irr
ATHDFS_J223221.4-602629	1.20	0.70	Scd
ATHDFS_J223400.9-602633	0.37	0.31	E/S0
ATHDFS_J223212.4-602632	0.78	0.73	Sbc
ATHDFS_J223136.2-602627	0.60	0.51	Sbc
ATHDFS_J223432.6-602614	1.15	-	—
ATHDFS_J223335.3-602615	0.08	0.09	E/S0
ATHDFS_J223136.9-602610	0.60	0.49	Sbc
ATHDFS_J223442.5-602601	0.40	0.40	Irr
ATHDFS_J223148.3-602554	0.57	0.43	Scd
ATHDFS_J223357.8-602548	0.01	0.03	Scd
ATHDFS_J223222.4-602532	-	0.46	E/S0
ATHDFS_J223351.2-602519	0.60	0.44	Sbc
ATHDFS_J223141.1-602506	0.19	0.31	Scd
ATHDFS_J223134.5-602457	0.37	0.56	Sbc
ATHDFS_J223317.1-602427	-	0.07	SB2
ATHDFS_J223444.9-602417	-	0.08	Scd
ATHDFS_J223436.8-602426	0.54	0.38	Scd
ATHDFS_J223245.3-602407	-	0.49	Sbc
ATHDFS_J223343.4-602348	0.14	0.20	SB2
ATHDFS_J223331.6-602307	-	0.59	E/S0
ATHDFS_J223358.9-602258	0.04	-	—
ATHDFS_J223300.5-602225	0.51	0.43	Scd
ATHDFS_J223154.6-602211	0.82	0.97	Sbc
ATHDFS_J223353.6-602136	-	0.91	Sbc
ATHDFS_J223341.1-602054	1.02	-	—
ATHDFS_J223431.4-602041	-	0.31	E/S0
ATHDFS_J223356.6-601949	0.27	0.21	E/S0
ATHDFS_J223316.0-601939	0.45	0.42	E/S0

ATHDFS name	$S_{1.4\text{GHz}}$	I mag	R_I
ATHDFS_J223353.9-605452	5.918	21.23	2.88
ATHDFS_J223214.8-605430	18.601	21.58	3.52
ATHDFS_J223448.4-605417	1.396	22.11	2.61
ATHDFS_J223203.0-605242A	87.888	21.59	4.20
ATHDFS_J223107.4-604855	11.272	21.86	3.42
ATHDFS_J223320.1-604457	0.344	24.90	3.12
ATHDFS_J223210.3-604433	56.513	19.46	3.16
ATHDFS_J223534.3-604328	0.657	23.66	2.90
ATHDFS_J223355.6-604315	154.700	22.15	4.67
ATHDFS_J223123.1-603903	23.988	22.87	4.15
ATHDFS_J223245.6-603857	0.843	23.39	2.90
ATHDFS_J223404.8-603732	3.238	21.60	2.77
ATHDFS_J223343.7-603651	0.070	25.51	2.67
ATHDFS_J223350.5-603503	1.252	23.08	2.95
ATHDFS_J223420.9-603336	4.328	21.74	2.95
ATHDFS_J223212.9-603234A	2.816	22.02	2.88
ATHDFS_J223212.9-603234B	1.466	22.02	2.59
ATHDFS_J223113.5-603147	0.831	23.02	2.75
ATHDFS_J223329.1-602933	0.261	25.77	3.34
ATHDFS_J223444.9-602417	9.581	23.58	4.03
ATHDFS_J223245.3-602407	0.469	24.17	2.96
ATHDFS_J223303.6-605751	0.508	>23.5	>2.53
ATHDFS_J223410.5-605545A	2.106	>23.5	>3.14
ATHDFS_J223410.5-605545B	2.443	>23.5	>3.21
ATHDFS_J223308.5-605544	3.643	>23.5	>3.38
ATHDFS_J223317.5-605416A	7.754	>23.5	>3.71
ATHDFS_J223317.5-605416B	5.570	>23.5	>3.57
ATHDFS_J223403.1-605101	12.043	>23.5	>3.90
ATHDFS_J223454.0-604904	0.483	>23.5	>2.50
ATHDFS_J223527.8-604639B	1.423	>23.5	>2.97
ATHDFS_J223319.1-604348	1.085	>23.5	>2.86
ATHDFS_J223427.3-604258	0.571	>23.5	>2.58
ATHDFS_J223417.8-604009	1.502	>23.5	>3.00
ATHDFS_J223429.9-603629	0.671	>23.5	>2.65
ATHDFS_J223224.0-603537	1.259	>23.5	>2.92
ATHDFS_J223258.5-603346	1.010	>23.5	>2.82
ATHDFS_J223509.5-603257	0.980	>23.5	>2.81
ATHDFS_J223537.7-603013	2.860	>23.5	>3.28
ATHDFS_J223236.5-603000	1.507	>23.5	>3.00
ATHDFS_J223355.5-602956	1.534	>23.5	>3.01
ATHDFS_J223140.6-602924	4.962	>23.5	>3.52
ATHDFS_J223117.4-602850	7.756	>23.5	>3.71
ATHDFS_J223306.6-602425	1.949	>23.5	>3.11
ATHDFS_J223410.2-602324	0.582	>23.5	>2.58

Table 12: Summary of ATHDFS sources deemed radio-loud from the radio-to-optical ratio.